8 Electromagnetic induction

The electromagnetic (EM) induction method, traditionally used for mining, groundwater, and geothermal exploration and geological mapping (Grant and West, 1965; Nabighian, 1988; 1991), is growing in popularity for near-surface geophysical applications (McNeill, 1990; Nobes, 1996; Tezkan, 1999; Pellerin, 2002; Fitterman and Labson, 2005; Everett, 2012). The controlled-source variant of the method utilizes low-frequency (~ 1–100 kHz) time variations in electromagnetic fields that originate at or near the surface and diffuse into the subsurface. The ground-penetrating radar (GPR) technique is distinct from the EM induction method in the sense that the former utilizes a higher frequency range > 1 MHz for which wave propagation, rather than diffusion, is the dominant energy transport mechanism. The diffusive regime is marked by the requirement $\sigma >> \omega\varepsilon$ where σ [S/m] is electrical conductivity, ω [rad/s] is angular frequency, and ε [F/m] is dielectric permittivity. The latter plays no physical role in the EM induction method. Instead, EM induction measurements respond almost entirely to the bulk subsurface electrical conductivity and, in particular, the spatial distribution of highly conductive zones (Everett, 2005). Instrumentation is readily available, easy to use, and reliable. Electric fields are sensed by pairs of grounded electrodes, i.e.voltmeters, while time-variations of magnetic fields are most commonly sensed using induction coils.

8.1 Introduction

The electrical conductivity structure of the subsurface, as determined from EM induction measurements, can be interpreted in the context of a wide variety of potential targets and application areas, see Table 8.1. Fundamentally, EM methods respond with good sensitivity to fluid type, clay content, and porosity. An overview of the physical and chemical factors that control the bulk electrical conductivity of geomaterials is provided by Gueugen

Table 8.1 Application areas and targets of EM induction geophysics.

Resistive targets	Intermediate targets	Conductive targets
Permafrost zones	Faults, fracture zones	Seawater intrusion
Aggregate deposits	Archaeological structures	Saline and inorganic plumes
Crystalline rock	Precision agriculture	Clay lenses, claypan soils
Caves, karst	Freshwater aquifers	Pipelines, steel drums, UXO

and Palciauskas (1995). The two case histories that follow serve as an introduction to the use of airborne and ground-based EM methods in near-surface investigations.

Example. Airborne EM mapping of a saline plume.

Soil and groundwater salinization negatively affects agriculture, water supplies, and ecosystems in arid and semi-arid regions worldwide. In Texas, especially before the 1960s and the tightening of environmental regulations, subsurface brines produced during oilfield drilling activities were frequently discharged into surface disposal pits which subsequently leaked their contents into the groundwater. Electromagnetic geophysical methods are capable of mapping conductive saline water concentrations, which are typically $\sigma \sim 0.1$–1.0 S/m, that invade geological backgrounds of $\sigma \sim 0.001$–0.01 S/m. Paine (2003) describes airborne EM mapping of such an oilfield brine plume in Texas (Figure 8.1). The plume is associated with a large area barren of vegetation that formed on a Pleistocene alluvial terrace of the Red River in the 1980s.

A helicopter EM system was employed consisting of coplanar horizontal coils and coaxial vertical coils flown at ~ 30 m altitude and operating at several frequencies between 0.9 and 56 kHz. The survey was performed with 100-m flight-line spacing and ~ 3 m along-track station spacing. A map of the 7.2 kHz apparent conductivity (Figure 8.1) clearly reveals the spatial extent of highly conductive ground. Many of the high-conductivity anomalies coincide with known brine-pit locations. The highest conductivity coincides with the barren area, which is bounded to the east by a topographic step to the Permian upland. The electromagnetic geophysical anomalies also find good spatial correlation with total dissolved solid (TDS) analyses based on sampled waters from monitoring wells distributed throughout the study area. The inferred boundary of the brine plume is marked on the map.

Example. Seawater intrusion in a coastal aquifer.

The intrusion of seawater into coastal freshwater aquifers is a serious problem in many places throughout the world. Human activities such as urbanization and the building of large-scale engineering projects such as dams can produce unintended negative effects on the hydrogeolgical conditions of coastal aquifers. Consequently it is important to develop methods that can identify the location of the freshwater–seawater interface. Electromagnetic geophysical methods offer an inexpensive and non-invasive alternative to drilling test boreholes. The electromagnetic detection of seawater is based on its high electrical conductivity relative to freshwater.

A ground-based electromagnetic geophysical survey of the Motril–Salobreña aquifer on the Mediterranean coast in southern Spain is reported by Duque *et al*. (2008). The geological setting is shown in Figure 8.2. The aquifer consists of Quaternary detrital sediments overlying Paleozoic and Mesozoic carbonates and metamorphics. As shown in the figure, a large dam is scheduled for construction along the Guadalfeo River that recharges the aquifer.

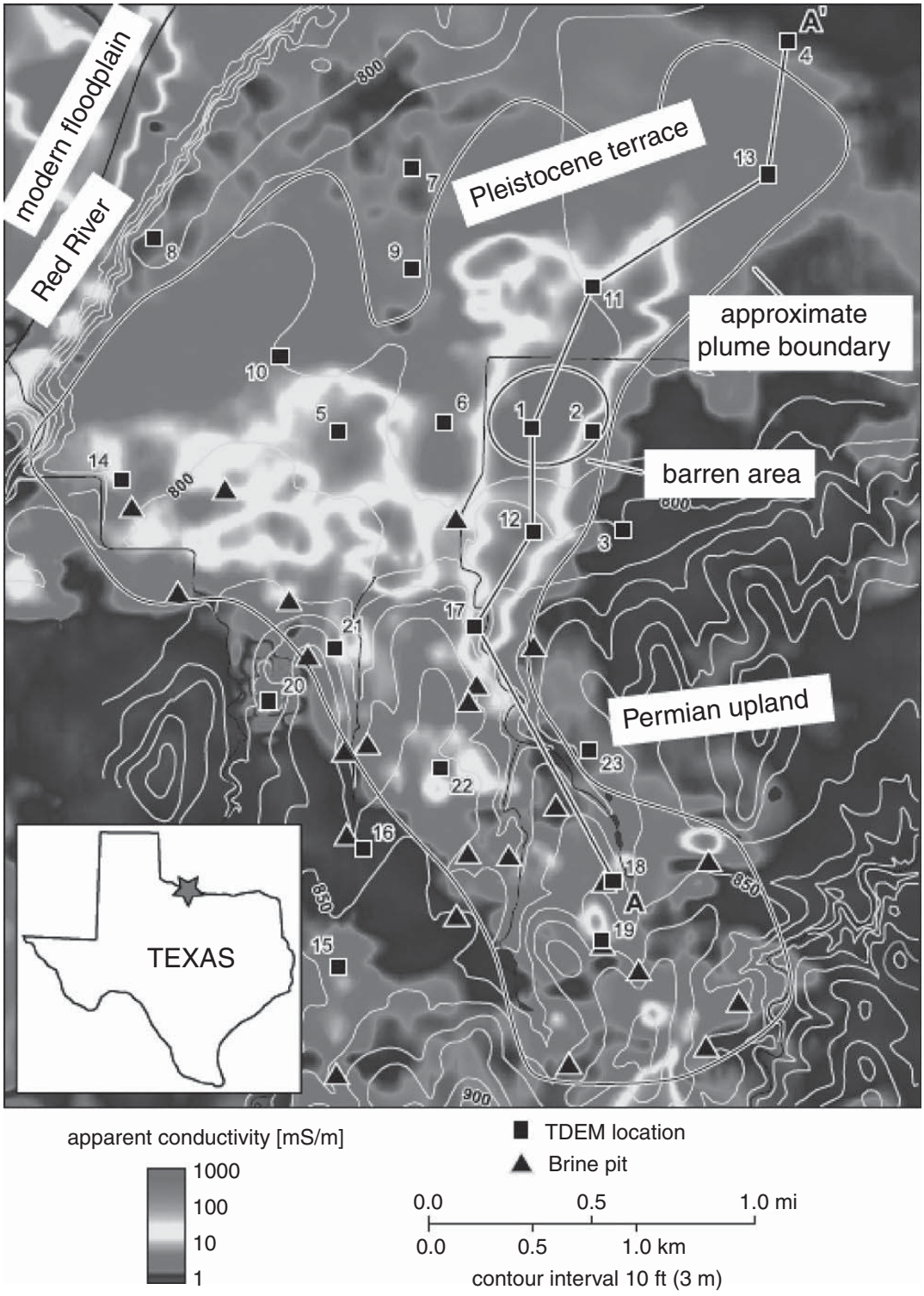

Figure 8.1 Topography and apparent resistivity at 7.2 kHz from airborne EM mapping of a north Texas oilfield brine plume. After Paine (2003).

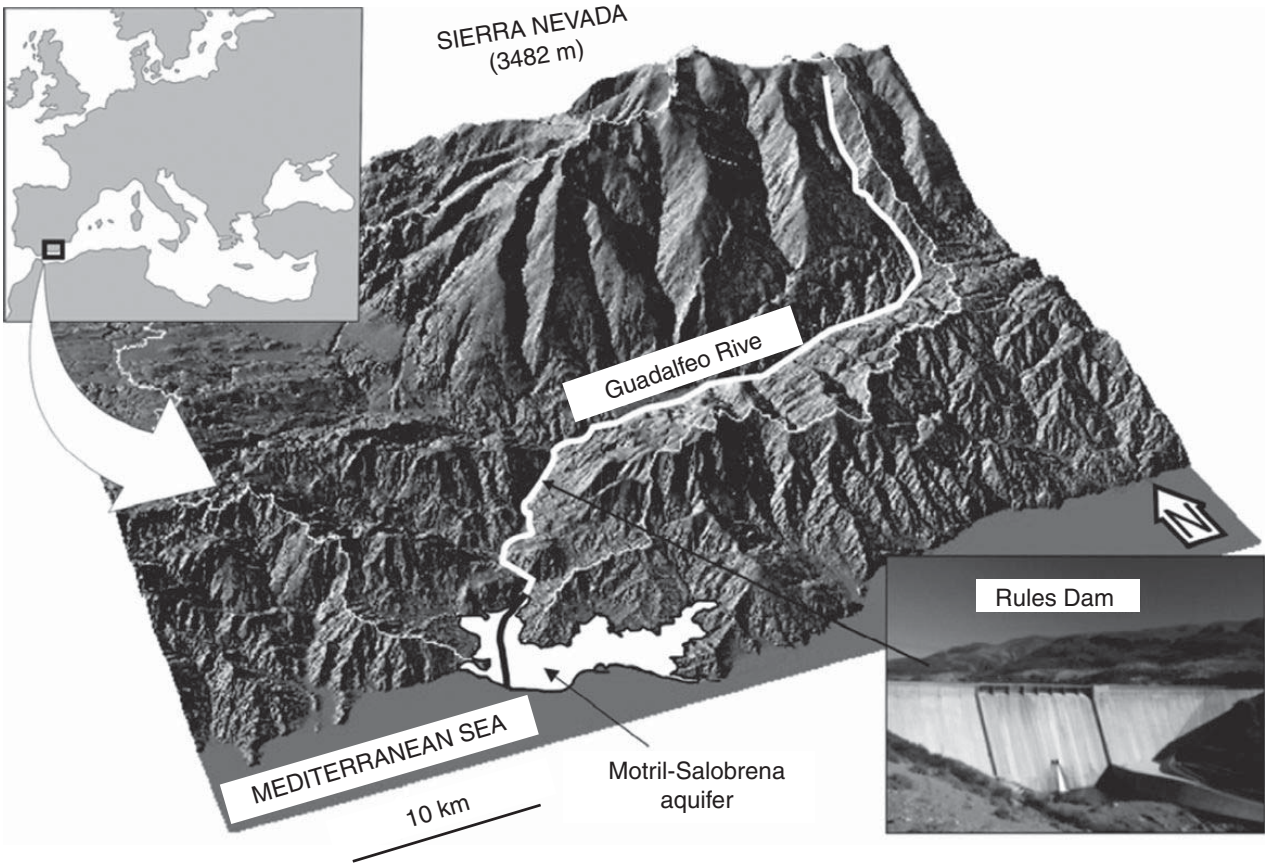

Figure 8.2 Geological setting of the Motril–Salobreña coastal aquifer (the white region) in Spain. After Duque *et al*. (2008).

The time-domain electromagnetic geophysical survey employed a central-loop configuration with transmitter loop sizes 50–200 m and consisted of several coast-perpendicular transects of ~ 2 km in length with station spacing of ~ 100–200 m. Plane-layered inversions of the measured transient responses were performed using a commercial software package; the resulting one-dimensional (1-D) conductivity depth-profiles were "stitched together" to form quasi-2-D depth-sections ready for interpretation. Two representative interpreted depth sections appear in Figure 8.3. The interpretations are based on conductivity assignments of $\sigma \sim 0.2$–2.0 S/m for seawater-saturated sediments; $\sigma \sim 0.003$–0.2 S/m for freshwater-saturated sediments; and $\sigma < 0.003$ S/m for the basement rocks. The location of the basement is further constrained by complementary gravity and borehole data. The results indicate that seawater intrusion into the near-surface aquifer is minor, with the marine wedge extending not more than 500 m inland. However, the position of the seawater–freshwater interface should be monitored carefully in the future owing to the impending urbanization and development of this coastal area. This case study shows that electromagnetic geophysical methods can play an important role in determining the spatiotemporal dynamics of the seawater–freshwater interface.

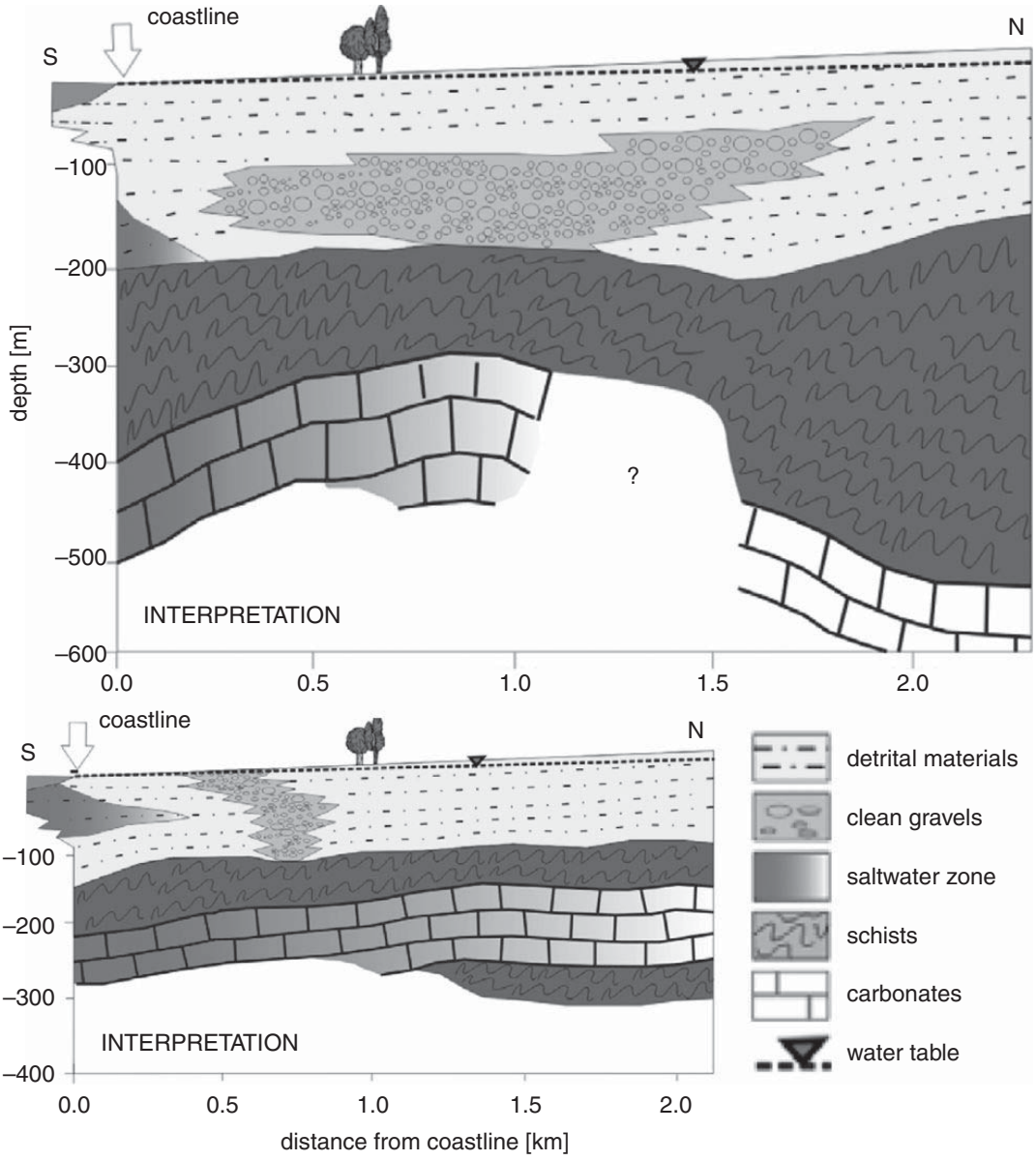

Figure 8.3 Interpretations of central-loop time-domain EM soundings in terms of seawater intrusion (red-colored areas) into the coastal Motril–Salobreña aquifer of southern Spain. After Duque *et al*. (2008).

8.2 Fundamentals

The electromagnetic geophysical method is founded on Maxwell's equations of classical electromagnetism. Standard physics textbooks such as Wangsness (1986) and Jackson (1998) are notable for their pedagogical, yet rigorous development of this topic. These texts however emphasize wave propagation rather than EM induction. The older books by Stratton (1941), Jones (1964), and Smythe (1967) treat induction in more detail and are highly recommended for advanced study. The reader is also referred to West and Macnae (1991) for a tutorial on the basic physics of induction.

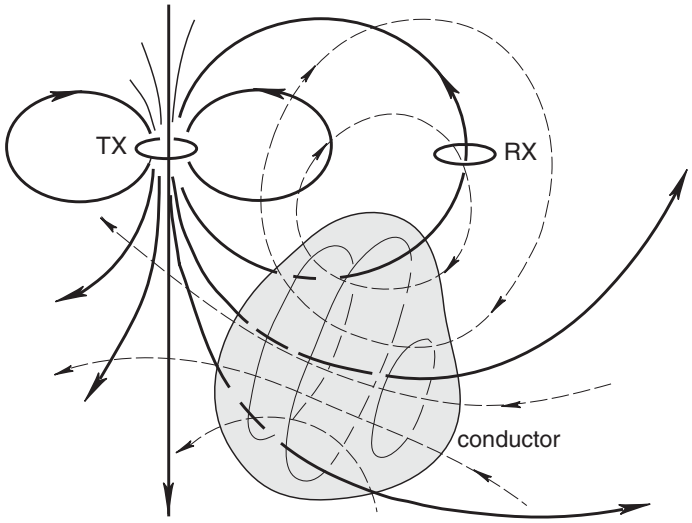

Figure 8.4 A sketch illustrating loop–loop electromagnetic target prospecting. After Grant and West (1965).

Controlled sources used by electromagnetic geophysicists may be either of the *grounded* type, as typified by the electric dipoles used in the resistivity method, or of the *inductive* type in which direct electrical contact with the ground is avoided by using an insulated wire-loop source. In the latter case, the source–ground coupling is achieved entirely by magnetic-flux linkage. The basic principles of inductive loop–loop electromagnetic prospecting for a conductive target are illustrated in Figure 8.4 and explained below.

A time-dependent electric current flowing in the transmitter (TX) coil generates a transient primary field $\mathbf{B}^P(\mathbf{r}, t)$, as shown schematically by the dark solid lines in the figure. A certain number of primary field lines flux through the conductive target, as indicated. This time-varying flux generates an electromotive force which causes eddy currents (light solid lines) of density $\mathbf{J}(\mathbf{r}, t)$ to flow in the conductor. The eddy currents, in turn, generate a secondary magnetic field $\mathbf{B}^S(\mathbf{r}, t)$, as shown by the dashed lines, that is characteristic of the target geometry, and its position and conductivity. Both primary and secondary field lines flux through the RX coil, as shown. Consequently, a voltage is induced in the RX coil containing both the primary signal from the TX and the secondary electromagnetic response of the target. Since the primary signal is known, depending only on the TX–RX configuration, it can be removed, leaving only the unknown target response.

As further aid to understand the EM method, it is worthwhile to recall that the geological medium under investigation, including a conductive target and its host, is considered to be electrically neutral. The investigated volume contains a huge number but roughly equal amounts of positive and negative charge carriers. Some of the charge carriers are mobile and may migrate or drift from place to place within the medium while other charge carriers are essentially fixed in place, bound to lattice atoms or to material interfaces. The EM induction method is concerned only with the mobile charges.

An elementary description of EM induction starts with the Lorentz force $\mathbf{F} = q(\mathbf{E} + \mathbf{v}\times\mathbf{B})$, which is experienced by a mobile charge carrier q moving with velocity $\mathbf{v}$ in an electromagnetic field ($\mathbf{E}$, $\mathbf{B}$). An amount of work ε is done by the electromagnetic field on the charge carrier as it completes one cycle of an arbitrary closed path L. The quantity ε is

called the electromotive force, or *emf*. The emf is not a force per se but rather a voltage or equivalently a potential. Essentially, a voltage develops along any arbitrary closed path L within a conducting body that is exposed to a time-varying **B** magnetic field. The field variations may be naturally occurring but in the controlled-source electromagnetic (CSEM) method, it is the geophysicist who shapes the external time variation with the aid of a transmitter.

The velocity **v** in the expression for the Lorentz force is interpreted as the charge-carrier *drift velocity* $\mathbf{v}_d$. Mobile charge carriers in conducting bodies migrate with an average drift velocity $\mathbf{v}_d$ in response to an applied electric field. The drift velocity satisfies $|\mathbf{v}_d| << c$, where c is the speed of light, the low velocity being due to lattice scattering of the charge carriers as they migrate. The drift velocity of electrons in standard 14-gauge copper wire carrying a 1 A current, for example, is just $|\mathbf{v}_\mathrm{d}| \sim 40$ μm/s (Tipler, 1982). The ions of an electrolyte solution are even less mobile. The mobilities of Na^+ and Cl^- ions in seawater at temperature $T = 25$ °C are $m_+ \sim 5 \times 10^{-8}$ m^2/V s and $m_- \sim 8 \times 10^{-8}$ m^2/V s, respectively (Conway and Barradas, 1956). Since $\mathbf{v}_d = m\mathbf{E}$, this implies a very small drift velocity of $\sim 10^{-13}$ m/s in a typical electric field strength of ~ 1 mV/km.

An electric current density is associated with the drift velocity as $\mathbf{J} = nq\mathbf{v}_d$, where n is the volumetric concentration of the charge carrier. The electrical conductivity is related to the density and mobility of the charge carrier by $\sigma = nqm$ (Kittel, 1968; Gueugen and Palciauskas, 1995). Notice that an appreciable induced current does not flow in an insulator such as oil or epoxy since, in these materials, the number density n of mobile charges is negligible. It is the induced drift of mobile charges or eddy current **J**, acting as a secondary source of electromagnetic field, that generates the electromagnetic response measured by geophysicists.

In addition to the mobile charges that are present in conductive geomaterials, there certainly also exist *bound charges* that are not able to drift freely but nevertheless experience the Lorentz force **F** in the presence of an applied electromagnetic field. The motion of these bound charges leads to several types of *polarization*, foremost of which are atomic and molecular polarization, as earlier discussed in connection with the induced polarization (IP) method. Other types of bound-charge motion are also possible, but none of these are of direct relevance to the CSEM method. In other words, neither the bound charges that are confined to individual atoms, nor the mobile charges that are trapped at material interfaces, make any signficant contribution to the EM induction response. Such motions are capacitive effects; as shown in the next chapter, they are a very important aspect of the ground-penetrating radar (GPR) technique.

8.3 The skin effect

The depth of penetration of the EM induction method is limited by the efficiency of the conversion of the transmitted electromagnetic energy into kinetic energy of the mobilized subsurface charge carriers. The higher the electrical conductivity σ, the greater the efficiency and consequently the smaller the depth of penetration. The well-known *skin effect*

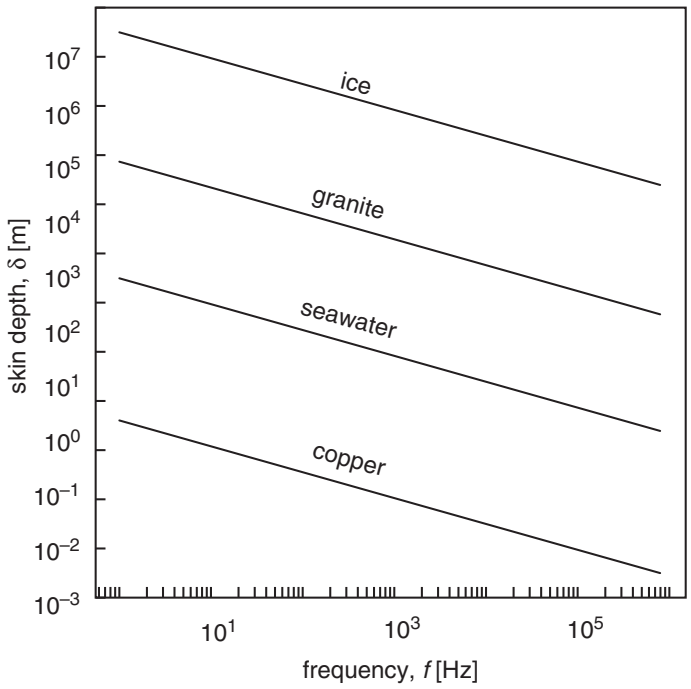

Figure 8.5 Skin depth as a function of frequency for several important non-magnetic geomaterials.

states that normally incident plane-wave signals lose $1/e \sim 0.368$ of their incident amplitude after penetrating one skin depth δ into a medium of conductivity σ,

$$\delta = \sqrt{\frac{2}{\mu\sigma\omega}}, \tag{8.1}$$

where μ is magnetic permeability, $\omega = 2\omega f$ is the transmitted frequency, and $e \sim 2.71828$ is the base of the natural logarithm, that is, $e = \exp(1)$.

In the EM method, the magnetic permeability is almost always assumed to be equal to its free space value, $\mu = \mu_0$, even in the presence of magnetite-bearing rock formations. An important exception to this rule occurs if compact ferrous metal targets, such as pipelines, steel drums, or unexploded ordnance (UXO), are being investigated (e.g. Pasion, 2007) in which case $\mu \sim 1.05\mu_0$–$50\mu_0$, or even higher. To explore the depth of penetration in some common non-magnetic geomaterials, typical values found in the literature for conductivity can be used: $\sigma \sim 10^{-9}$ S/m (ice); $\sigma \sim 10^{-4}$ S/m (granite); $\sigma \sim 3.2$ S/m (seawater); and $\sigma \sim 10^{6}$ S/m (copper). The graphs of $\delta(f)$ for these materials appear in Figure 8.5.

For loop-source excitation, the skin effect remains but the field distribution inside the Earth becomes more complicated due to the compact nature of the source. The electric-field intensity associated with diffusion from a loop source into a uniformly conducting halfspace is shown, in the frequency domain, in Figure 8.6a. The contours are shown in a vertical plane passing through the center of loop. Considering the azimuthal symmetry of the problem, the electric-field intensity takes on the appearance of a toroidal "smoke ring." The position of the maximum smoke-ring intensity in terms of the skin depth δ, as given by Equation (8.1), is shown in Figure 8.6b.

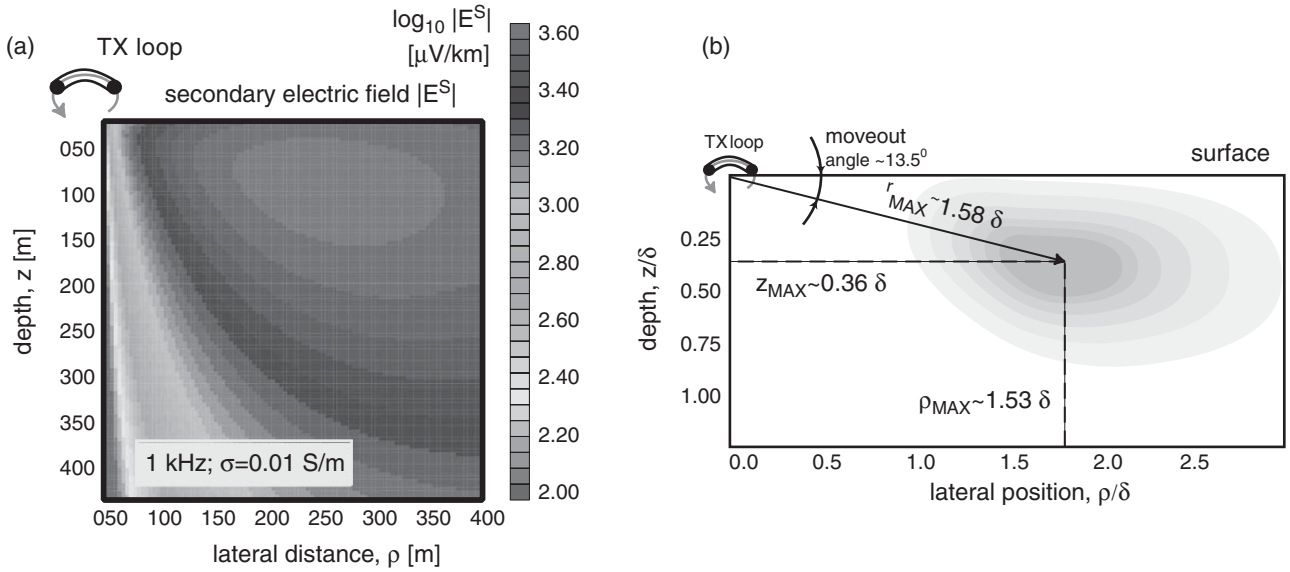

Figure 8.6 (a) Electric-field intensity due to loop excitation in a unform halfspace; (b) position of maximum intensity of the electric field in terms of skin depth.

8.4 Inductively coupled *LR* circuits

Considerable insight into the physics of an electromagnetic geophysical prospecting system may be gained by analyzing the behavior of a roughly equivalent system of three inductively coupled *LR* circuits (Grant and West, 1965), as shown below in Figure 8.7. In the equivalent system, the TX loop is modeled as *LR* circuit 1 with resistance R_1 and self-inductance L_1. Similarly, the RX coil is modeled as circuit 2 with its own resistance and self-inductance, respectively R_2 and L_2. The conductive body, which could represent a compact target such as an ore body or a UXO, or even an entire halfspace, is modeled by circuit 3 with (R_3, L_3), as shown.

Let us first examine the primary interaction between the TX loop and the RX coil in free space without the presence of the Earth/target. The *mutual inductance* between the TX and the RX circuits is given by M_{12}. In general, given two loops i and j, the mutual inductance M_{ij} is defined as the magnetic flux that passes through loop j due to a unit electric current flowing in loop i. Thus, mutual inductance is purely a geometric parameter that depends on the relative orientation and location of the two loops with respect to each other. Notice also that $M_{ij} = M_{ji}$. The *self-inductance* L_i is the magnetic flux that passes through loop i caused by unit current flow in the same loop, hence, $L_i = M_{ii}$.

Suppose Φ_j is the magnetic flux through loop j, defined according to

$$\Phi_j = \int_A \mathbf{B}_j \cdot \hat{\mathbf{n}} dA, \tag{8.2}$$

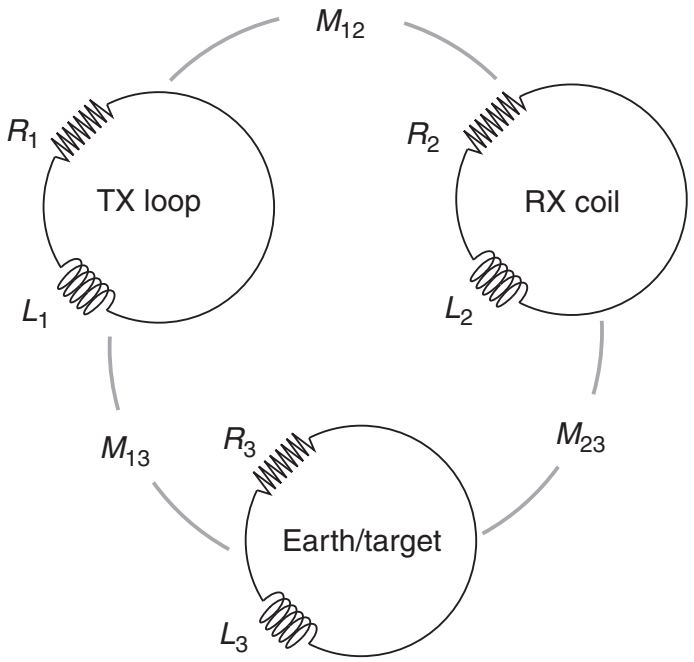

Figure 8.7 Electromagnetic prospecting system conceptualized as inductively coupled *LR* circuits.

where an element of the area A of the loop is denoted by dA and $\hat{\mathbf{n}}$ is the unit normal vector oriented along the axis of the loop. The loop need not be planar, it can be bent or twisted in which case the unit normal vector would depend on location, $\hat{\mathbf{n}} = \hat{\mathbf{n}}(r)$. The magnetic field flowing through loop j is denoted as $\mathbf{B}_j$, which presumably is caused by a current I_i flowing in some other loop i. By the definition of mutual inductance, we have

$$\Phi_j = M_{ij} I_i. \tag{8.3}$$

The magnetic, or inductive, coupling of the two loops is embodied in the empirical law generally attributed to Faraday stating that the negative rate of change of flux though a loop equals the voltage V_j induced in the loop, or

$$V_j = -\frac{d\Phi_j}{dt} = -M_{ij}\frac{dI_i}{dt}. \tag{8.4}$$

The above equation reveals that a voltage is induced in loop j if the current flow in loop i is changing with time. Suppose the time variation in the current I_i is harmonic such that $I_i \sim \exp(i\omega t)$ where ω is the angular frequency, then from Equation (8.4) the induced voltage in loop j in the frequency domain is

$$V_j = -i\omega M_{ij} I_i. \tag{8.5}$$

To completely describe the magnetic coupling of two current loops i and j, we need two other empirical laws of classical electromagnetism. The first is a simplified (neglecting radiation effects) version of the Biot–Savart law which, for our purposes, reads

$$\mathrm{B}_j = K_j I_j, \tag{8.6}$$

stating that the magnitude of $B_j = |\mathbf{B}_j|$ of the magnetic field generated by the induced current in loop j is proportional to the strength of the current I_j and completely in phase with it. The constant of proportionality K_j is a geometric factor that depends on the shape, size, and number of turns, of loop j. The second fundamental law is Ohm's law, which, for a general LR circuit in the time domain, is $V(t) = I(t)R + L\partial I(t)/\partial t$, while in this particular time-harmonic case it becomes

$$V_j = I_j[R_j + i\omega L_j]. \tag{8.7}$$

Putting the previous expressions together, we can easily see that the *primary* magnetic field measured by RX loop 2 in Figure 8.6 due to current flow in the TX loop is

$$\mathrm{B}^P = -\frac{i\omega K_2 M_{12} I_1}{R_2 + i\omega L_2}. \tag{8.8}$$

Now, let us add the third loop into the system to incorporate the effect of the conductive Earth or buried target. The voltage induced in the Earth/target loop 3 follows as in Equation (8.5) from Faraday's law and the definition of mutual inductance,

$$V_3 = -i\omega M_{13} I_1, \tag{8.9}$$

to which Ohm's law, Equation (8.7), can be applied to find the induced current I_3 in the ground circuit,

$$I_3 = \frac{V_3}{R_3 + i\omega L_3} = -\frac{i\omega M_{13} I_1}{R_3 + i\omega L_3}. \tag{8.10}$$

The induced current I_3 in the ground in turn generates a secondary voltage signal V_2^S in the RX loop 2 which can be found by another application of Faraday's and Ohm's laws,

$$V_2^S = -i\omega M_{23} I_3 = -\frac{\omega^2 M_{13} M_{23} I_1}{R_3 + i\omega L_3}. \tag{8.11}$$

The secondary induced current I_2^S in the RX loop due to the current flowing in the ground circuit is therefore given by

$$I_2^S = \frac{V_2^S}{R_2 + i\omega L_2} = -\frac{\omega^2 M_{13} M_{23} I_1}{(R_2 + i\omega L_2)(R_3 + i\omega L_3)}. \tag{8.12}$$

Hence, the *total* magnetic field B_2 measured by the RX loop is given by the simplified - Biot–Savart law applied to the summation of the primary and secondary induced currents,

$$\mathrm{B}_2 = K_2(I_2 + I_2^S) = -\frac{i\omega K_2 M_{12} I_1}{R_2 + i\omega L_2} - \frac{\omega^2 K_2 M_{13} M_{23} I_1}{(R_2 + i\omega L_2)(R_3 + i\omega L_3)}, \tag{8.13}$$

which reduces to

$$\mathrm{B}_2 = \frac{K_2 I_1}{R_2 + i\omega L_2}\left\{-i\omega M_{12} - \frac{\omega^2 M_{13} M_{23}}{R_3 + i\omega L_3}\right\}, \tag{8.14}$$

or

$$B_2 = B_0\{\Gamma^P + \Gamma^S\}. \tag{8.15}$$

In the above equation, the pre-factor $B_0 = K_2 I_1/(R_2 + i\omega L_2)$ is a known term that depends only on the TX current I_1 and the various geometric properties of the RX loop, which are under the control of the experimenter. The first term in the curly brackets $\Gamma^P = -i\omega M_{12}$ is also known and depends only on the frequency ω and the mutual inductance of the TX and RX loops, both of which are under experimenter control. The second term in the curly brackets $\Gamma^S = -\omega^2 M_{13} M_{23}/(R_3 + i\omega L_3)$ depends on the *unknown* quantities M_{13} and M_{23}, which describe the relative orientation and location of the ground circuit with respect to the TX and RX loops. It also depends on the unknown parameters R_3 and L_3 which contain information about, respectively, the physical properties and the geometry of the ground circuit.

Examining the response of the Earth/target circuit, as a function of TX frequency ω, is important to better understand the EM induction geophysical method. To this end, based on the definition of Γ^P and Γ^S in Equation (8.15), we specify the *normalized response function* as

$$\frac{\Gamma^S}{\Gamma^P} = \kappa \frac{i\omega L_3/R_3}{1 + i\omega L_3/R_3} \tag{8.16}$$

where $\kappa = M_{13}M_{23}/M_{12}L_3$ is a factor that depends only on the geometry of the TX–target–RX configuration. The function Γ^S/Γ^P in Equation (8.16) captures the fundamental behavior of the electromagnetic response of the Earth or a compact buried target while suppressing complexities associated with the TX and RX loop geometries. To examine the frequency dependence of Γ^S/Γ^P we can set $\kappa = 1$ without obscuring the essential physics. A graph of Γ^S/Γ^P versus the normalized frequency, or *response parameter* $\omega L_3/R_3$, is shown in Figure 8.8. The real part

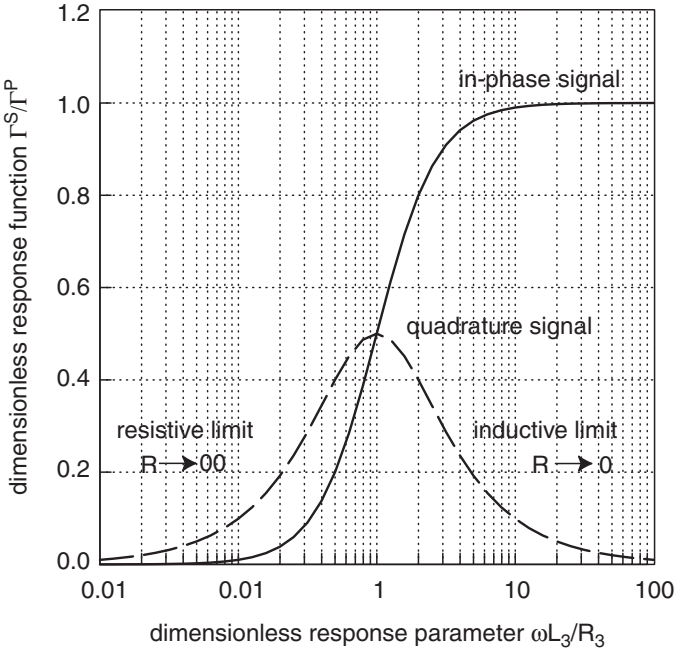

Figure 8.8 Idealized electromagnetic response of a buried target.

of the response function $\Gamma^S/\ \Gamma^P$ is termed the *in-phase signal* since its time variation coincides with that of the TX current. The imaginary part of $\Gamma^S/\ \Gamma^P$ is the out-of-phase, or *quadrature*, signal, so-called since its time variation is exactly 90° out of phase with the TX current.

There are three important frequency regimes in EM prospecting that are apparent from Figure 8.8. The low-frequency regime, in which $\omega L_3/R_3 << 1$, is termed the *resistive limit* and is achieved as the frequency $\omega \rightarrow 0$ or equivalently as the target resistance $R_3 \rightarrow \infty$. The high-frequency regime $\omega L_3/R_3 >> 1$, or *inductive limit*, is achieved as $\omega \rightarrow \infty$ or equivalently $R_3 \rightarrow 0$. Finally, there is an intermediate frequency range at which $\omega L_3/R_3 \sim 1$.

In the resistive limit, as indicated in Figure 8.8, the in-phase signal vanishes and the quadrature signal is small. The low amplitude of the EM response is expected since the target is very resistive and hence induction of an electric current in the ground circuit is poor. Since the response function is of the form $\Gamma^S/\Gamma^P \sim (i\omega L_3/R_3)/(1 + i\omega L_3/R_3)$ it is clear that, in the resistive limit, $\Gamma^S/\ \Gamma^P \rightarrow i\omega L_3/R_3$. This is a small, purely quadrature signal.

In the inductive limit, the EM response function tends to $\Gamma^S/\ \Gamma^P \rightarrow 1$ which indicates a large in-phase signal with the quadrature signal becoming very small. The reason that the EM response $\Gamma^S/\ \Gamma^P$ is amost entirely in-phase with the TX current is that there is an additional ~ 90° phase-shifting process that operates at the inductive limit compared to the resistive limit. Specifically, when $R_3 \rightarrow 0$, according to Equation (8.10), the current induced in the Earth target is shifted out of phase with respect to the voltage. In essence, induction is a "*d*/*dt process*." In the inductive limit, there are two additive *d*/*dt* processes at work; one generating the induced current in the target and the other generating the induced current in the RX coil. The superposition of the two *d*/*dt* processes explains why the inductive-limit EM response function is brought back into phase with the TX current.

As further shown in Figure 8.8, the quadrature signal peaks at an intermediate frequency range, $\omega L_3/R_3 \sim 1$. This result indicates that an EM prospecting system can generate a maximal target response, in the quadrature signal, over a specific range of frequencies. The EM quadrature response diminishes at both higher and lower frequencies. Clearly, there is a preferred band of frequencies centered on $\omega \sim R_3/L_3$ that is most useful for detecting the ground circuit. The existence of a preferred band is not surprising when it is recognized that there is a characteristic time for the decay of an electric current flowing in a simple *LR* circuit, namely $\tau = L/R$.

Fitterman and Labson (2005) have analyzed the transient response $V_2(t)$ of the coupled *LR*-circuit system for a step-off in the TX current, $I_1(t) = I_1[1 - u(t)]$, where $u(t)$ is the Heaviside step-on function. They showed that the RX signal $V_2(t)$ consists of a sudden initial rise followed by an exponential decay with time constant τ. A larger time constant, appropriate to describe currents that can flow readily in the Earth circuit, generates a smaller initial amplitude but produces a longer-lived decay of the RX signal. Further discussion of transient EM is deferred to Section 8.6.

8.5 Terrain conductivity meters

A simple electromagnetic geophysical reconnaissance tool is the terrain conductivity meter (McNeill, 1980). This frequency-domain instrument operates as a purely inductive system in which transmitter (TX) and receiver (RX) loops do not make electrical contact with the ground. The two loops are magnetically flux-linked to each other and to the conductive ground as shown schematically by the circuits in Figure 8.7. Two popular terrain conductivity meters are the Geonics EM31 and EM34 instruments shown in Figure 8.9. The EM31 operates at 9.8 kHz and has TX–RX intercoil spacing of 3.66 m. The EM34 has three different intercoil spacings: 10, 20, and 40 m; these operate at, respectively, 6.4, 1.6 and 0.4 kHz. The EM34 can be used with vertical coplanar coils (horizontal dipole, or HD mode), as shown in the figure, or horizonal coplanar coils (vertical dipole, or VD mode) in which case the coils are laid flat on the ground.

The operating principle of the terrain conductivity meter is based on classical EM induction theory. A time-harmonic current of the form $I(t) = I\sin(\omega t)$ is passed through the TX loop. The primary magnetic field due to the current flowing in the transmitter loop is in-phase with the current and consequently has the form

$$\mathbf{B}^P(\rho, t) = \mathbf{B}_0(\rho)\sin(\omega t), \tag{8.17}$$

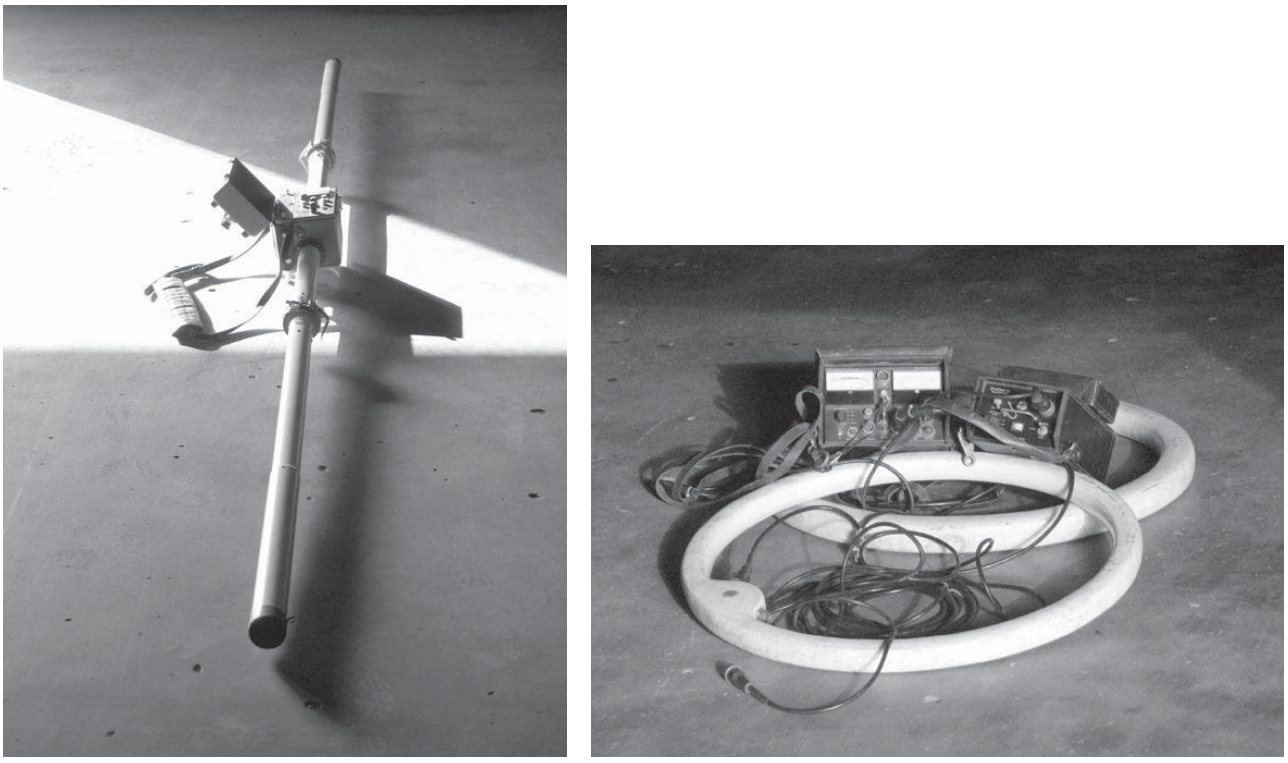

Figure 8.9 Terrain conductivity meters: (left) Geonics EM31; (right) Geonics EM34.

where ρ is the radial distance in a cylindrical coordinate system originated at the center of the TX loop. The conductive ground responds to the imposition of the time-varying primary magnetic flux by establishing a system of electromagnetic eddy currents whose secondary magnetic field $\mathbf{B}^S(\rho, t)$ is organized such that it tends to oppose the *change* $\partial\mathbf{B}^P/\partial t$ in primary flux. This principle was earlier captured in the circuit analogy by Equation (8.4). Essentially, the changing primary flux establishes an *electromotive force* (emf) in the ground. The ground then responds by generating a *back-emf* in an effort to restore the equilibrium that existed before the change occurred in the primary flux. This behavior accords with Lenz's law of electromagnetics, which (like homeostasis) is a specific case of Le Chatelier's principle in chemistry:

> If a system at equilibrium experiences a change of state, the equilibrium will shift in a direction so as to counter-act the imposed change.

The secondary magnetic field then has the form

$$\mathbf{B}^S(\rho, t) = \mathbf{B}_1(\rho)\sin(\omega t + \varphi). \tag{8.18}$$

where $|\mathbf{B}_1| << |\mathbf{B}_0|$, and φ is the phase shift caused by the induced currents which are not completely in-phase with the primary magnetic flux. The magnitude of the phase shift depends on the electrical conductivity of the ground. If the ground is perfectly conducting, $\varphi = 90^\circ$ and the secondary magnetic field is completely out of phase. If the ground is perfectly resistive, $\varphi = 0$ and the secondary magnetic field is completely in-phase. In general, the secondary magnetic field is *delayed* and *attenuated* with respect to the primary magnetic field, indicative of EM induction as an energy-dissipating d/dt process.

Using the identity

$$\sin(\omega t + \varphi) = \sin\omega t\cos\varphi + \cos\omega t\sin\varphi \tag{8.19}$$

we can decompose the total magnetic field $\mathbf{B}^T(\rho, t) = \mathbf{B}^P(\rho, t) + \mathbf{B}^S(\rho, t)$ into two orthogonal components:

$$\begin{aligned}\mathbf{B}^T(\rho, t) &= \mathbf{B}_0(\rho)\sin\omega t + \mathbf{B}_1(\rho)\sin(\omega t + \varphi)\\ &= \mathbf{B}_0(\rho)\sin\omega t + \mathbf{B}_1(\rho)\sin\omega t\cos\varphi + \mathbf{B}_1(\rho)\cos\omega t\sin\varphi\\ &= [\mathbf{B}_0 + \mathbf{B}_1\cos\varphi]\sin\omega t + [\mathbf{B}_1\sin\varphi]\cos\omega t\end{aligned} \tag{8.20}$$

such that $R = |\mathbf{B}_0 + \mathbf{B}_1\cos\varphi|$ is termed the *real* (*in-phase*) *response* and $Q = |\mathbf{B}_1\sin\varphi|$ is termed the *quadrature* (*out-of-phase*) *response*. The quantities (R, Q) are measured by the EM instrument. The quadrature signal is very small since in most cases,

$$\frac{|\mathbf{B}_1|}{|\mathbf{B}_0|} \sim 10^{-6} = 1\text{ppm}. \tag{8.21}$$

This implies that the strength of the induced current is only a very small fraction of the strength of the primary transmitted current, the latter being typically 1–3 A. The quadrature signal reveals information about the Earth since it vanishes ($Q = 0$) if the conductive Earth is not present. Notice that the known primary signal $\mathbf{B}_0$ can be subtracted to form a secondary in-phase response $R_S = |\mathbf{B}_1\cos\varphi|$. Instead of the real and quadrature

components, an EM system can also measure the *amplitude* and *phase* of the ground response. In terms of the quantities (R_S, Q), the amplitude is given by

$$A = \sqrt{R_S^2 + Q^2} = \sqrt{(\mathbf{B}_1 \cos\varphi)^2 + (\mathbf{B}_1 \sin\varphi)^2} = |\mathrm{B}_1|, \tag{8.22}$$

as required, while the phase is

$$\varphi = \tan^{-1}\frac{Q}{R_S} = \tan^{-1}\frac{\mathbf{B}_1 \sin\varphi}{\mathbf{B}_1 \cos\varphi} = \tan^{-1}(\tan\varphi) = \varphi \tag{8.23}$$

as required.

It is demonstrated below that the measured quadrature response Q can be interpreted in terms of the apparent ground conductivity σ_a. An *apparent conductivity* is defined as the conductivity of a homogeneous halfspace that would generate a quadrature response that is identical to the one that is observed. Keep in mind that $\sigma_a = \sigma_a(\omega)$ for an inhomogeneous geological formation since the signal penetration depth depends on frequency, according to the skin effect.

It can be shown that the normalized secondary vertical magnetic field ($b_z^{\mathrm{S}}/b_z^{\mathrm{P}}$) for coils operating in the VD mode over homogeneous ground, assuming a small horizontal TX loop such that loop radius $a/\rho << 1$, can be simplified to (Wait, 1954; McNeill, 1980):

$$\left(\frac{b_z^S}{b_z^P}\right)_V \approx -\frac{2}{\alpha^2\rho^2}\{9 - [9 - 9i\alpha\rho - 4\alpha^2\rho^2 + i\alpha^3\rho^3]\exp(i\alpha\rho)\}, \tag{8.24}$$

where $\alpha^2 = -i\mu_0\sigma\omega$. Furthermore, at low induction numbers,

$$\mathrm{B} \equiv \frac{\rho}{\delta} \ll 1, \text{ orequivalently, } |\alpha\rho| \ll 1, \tag{8.25}$$

such that the TX–RX separation distance is much less than the electromagnetic skin depth (equivalent also to low frequency), it is straightforward to show that Equation (8.24) reduces to

$$\left(\frac{b_z^S}{b_z^P}\right)_V \approx 1 - \frac{i\mu_0\omega\sigma\rho^2}{4}. \tag{8.26}$$

The VD-mode apparent conductivity σ_a is then obtained by re-arranging the out-of-phase component of Equation (8.26),

$$\sigma_a = \frac{4}{\mu_0\omega\rho^2}\left|\mathrm{Im}\left(\frac{b_z^S}{b_z^P}\right)\right|. \tag{8.27}$$

Similarly, when the TX and RX coils are oriented in the HD mode, the normalized secondary field is approximated by (McNeill, 1980)

$$\left(\frac{b_z^S}{b_z^P}\right)_H = 2\left\{1 + \frac{3}{\alpha^2\rho^2} - [3 - 3i\alpha\rho - \alpha^2\rho^2]\frac{\exp(i\alpha\rho)}{\alpha^2\rho^2}\right\}, \tag{8.28}$$

and an equation identical in form to Equation (8.27) holds for the HD-mode apparent conductivity.

To summarize, the terrain conductivity meter, e.g. Geonics EM31 or EM34, reads an apparent conductivity that is linearly related to the measured quadrature response by $\sigma_a = 4Q_N/\mu_0\omega\rho^2$ where $Q_N = |\mathrm{Im}(b_z^S/b_z^P)_V|$ or $Q_N = |\mathrm{Im}(b_z^S/b_z^P)_H|$ depending on whether the instrument is being used in the VD or the HD mode.

The above discussion describes the basic operating principle of low-induction-number (LIN) terrain conductivity meters. The meter will fail, or exhibit erratic behavior including displaying negative apparent conductivities, in resistive terrain if the conductivity is sufficiently low such that the quadrature response Q_N falls below the system noise level. Resistive geological materials cannot sustain strong systems of induced currents. The terrain conductivity meter generates stable readings in conductive terrains, for example, $\sigma \sim 0.001$–0.1 S/m, since in these cases the quadrature response is large compared to the system noise level. The meter may also report negative apparent conductivities in the vicinity of strong lateral heterogeneities, such as might be caused by pipelines or faults, as the assumption of a homogeneous ground that was used to derive Equation (8.24) is not applicable in these cases. Finally, in highly conductive terrains the low-induction number (LIN) assumption (8.25) breaks down and the apparent conductivity σ_a no longer scales linearly with the measured quadrature response Q_N. In such cases, a correction factor such as the one proposed by Beamish (2011) should be applied to better estimate the apparent conductivity.

Measurements using a LIN terrain conductivity meter were taken by geophysics undergraduate students over a buried natural-gas pipeline on Riverside campus at Texas A&M University. The results are shown in Figure 8.10. Data were taken along a profile crossing the pipeline, with a Geonics EM31 instrument resting on the ground. Two orientations of the EM31 instrument were used: the in-line (left), or *P-mode*, in which the TX and RX coils are aligned with the profile direction; and the broadside (right), or *T-mode*, in which the TX and RX coils are aligned perpendicular to the profile direction (i.e. parallel to the pipeline). It is easy to see that the pipeline generates a strong, repeatable EM31 anomaly with high signal-to-noise ratio, for both modes. Notice there are some unphysical negative apparent conductivities in the P-mode profile in the vicinity of the pipepline. The striking differences between the P-mode and T-mode signatures reflect the variation in mutual electromagnetic coupling between the TX coil, the subsurface target, and the RX coil caused by differences in the relative geometry of the two modes relative to the target. At the beginning and the end of the profiles, both sets of EM31 readings tend to values of ~ 60–70 mS/m, regardless of the orientation of the coils, reflecting the relatively homogeneous background soil conditions.

A more comprehensive analysis of the EM31 response to a highly conductive target was performed by Benavides and Everett (2005). In that study, which has applications to EM imaging in areas with high cultural noise, a number of steel drill pipes were laid out on the ground in the pattern shown in Figure 8.11a. The P-mode and T-mode responses are shown in Figure 8.11b and 8.11c, respectively. The line spacing is 1.0 m and station spacing is 0.25 m. The data were acquired along north–south profiles. It is evident that the pipes generate elongate, bimodal anomalies that are oriented in the direction of the TX–RX coils. The smallest target, the drill pipe collar (item 4), generates only a subtle anomaly in each mode. The anomalies are highlighted if the difference between the T-mode and the P-mode

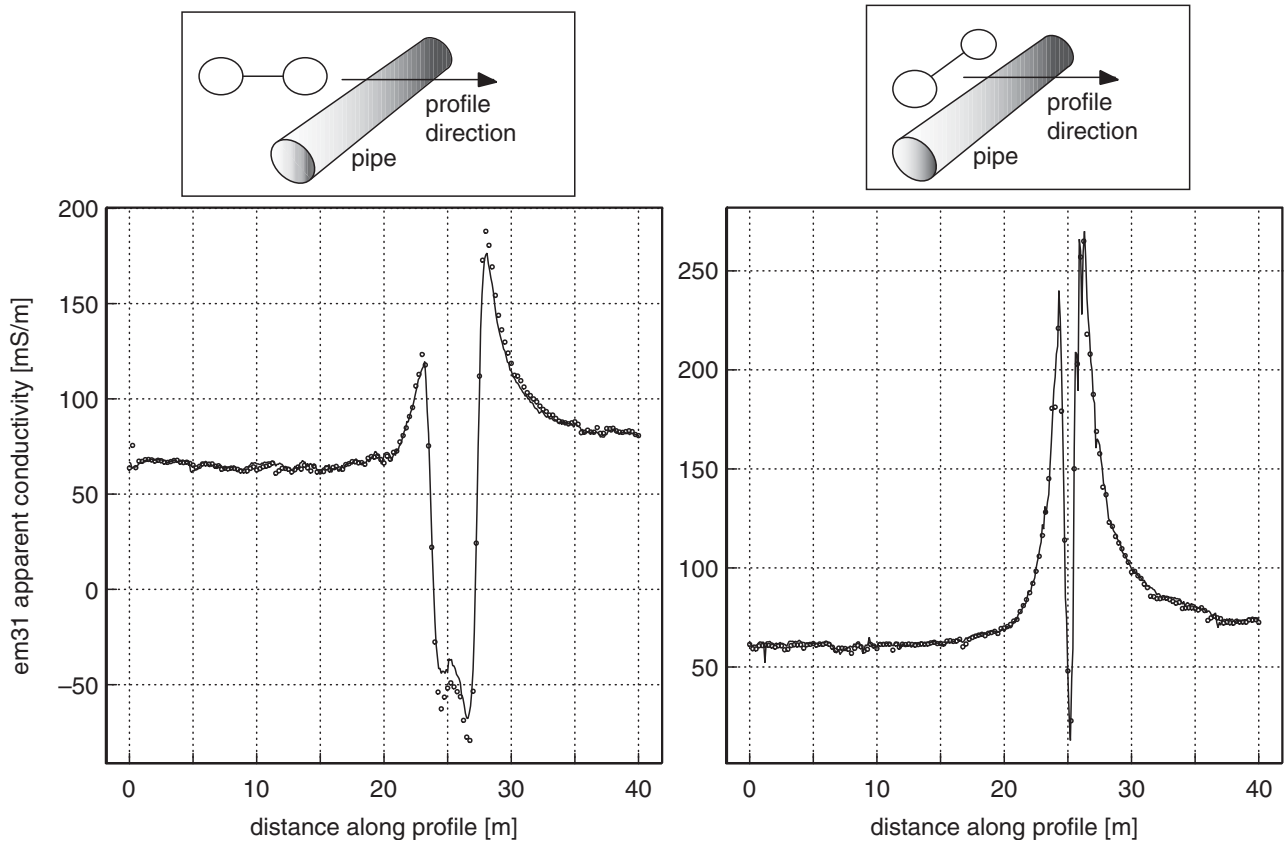

Figure 8.10 EM31 in-line P-mode (left side) and broadside T-mode (right side) signatures of the natural-gas pipeline at Texas A&M Riverside campus. Solid lines indicate original survey with 0.1-m station spacing. Symbols indicate repeat survey with 0.25-m station spacing.

signatures is plotted, as shown in Figure 8.10d. In this presentation, the pipe anomalies exhibit a distinctive quadrupole morphology, while the background soil response remains very subdued. Notice, however, that it is not easy to see from the geophysical signature that the drill pipe (item 5) is aligned at ~ 45° to the data-acquisition grid.

Terrain conductivity meters can also be used for mapping lateral contrasts in near-surface geology. Figure 8.12, left, illustrates EM34 readings taken with 10-m TX–RX intercoil spacing in the P-mode with the coil axes vertical (VD). The profile crosses a known lateral discontinuity juxtaposing a gravel unit with a sand/clay interbedded unit. The purpose of the survey was to delineate the extent of a paleochannel comprised of coarse sediment, in this case, an economic gravel deposit. Generally speaking, fine-grained material with abundant clay is more conductive than clean, coarse-grained sediment. The abrupt transition from low to high apparent conductivity marks the lateral boundary of the gravel paleochannel.

In Figure 8.12, right, the EM34 method (P-mode, VD) is used in its three different TX–RX intercoil spacings (10, 20, and 40 m) to map faults and stratigraphic contacts in a well-characterized consolidated sandstone aquifer in central Texas. The Hickory sandstone, of Cambrian age, is divided into lower, middle, and upper units. It is known that the faults and contacts act as barriers and conduits compartmentalizing groundwater flow in this aquifer.

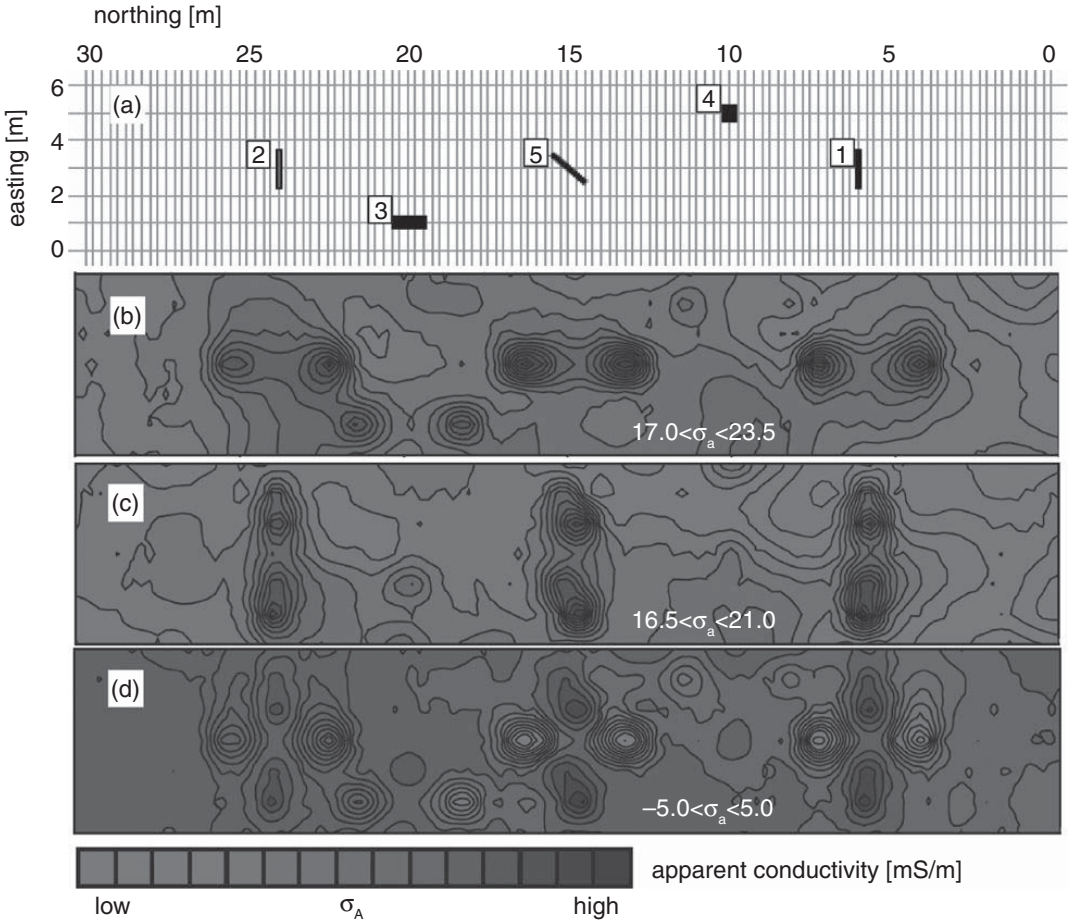

Figure 8.11 EM31 detection of conductive targets. (a) Experimental layout of steel pipes; (b) P-mode apparent conductivity map; (c) T-mode apparent conductivity map; (d) difference of the T-mode and P-mode maps; key: 1, 5 = 155 × 12.4-cm drill pipe, 2 = 150 × 6.4-cm drill pipe, 3 = 75 × 7.5-cm galvanized iron water pipe, 4 = 28 × 7.2-cm drill pipe collar. After Benavides and Everett (2005).

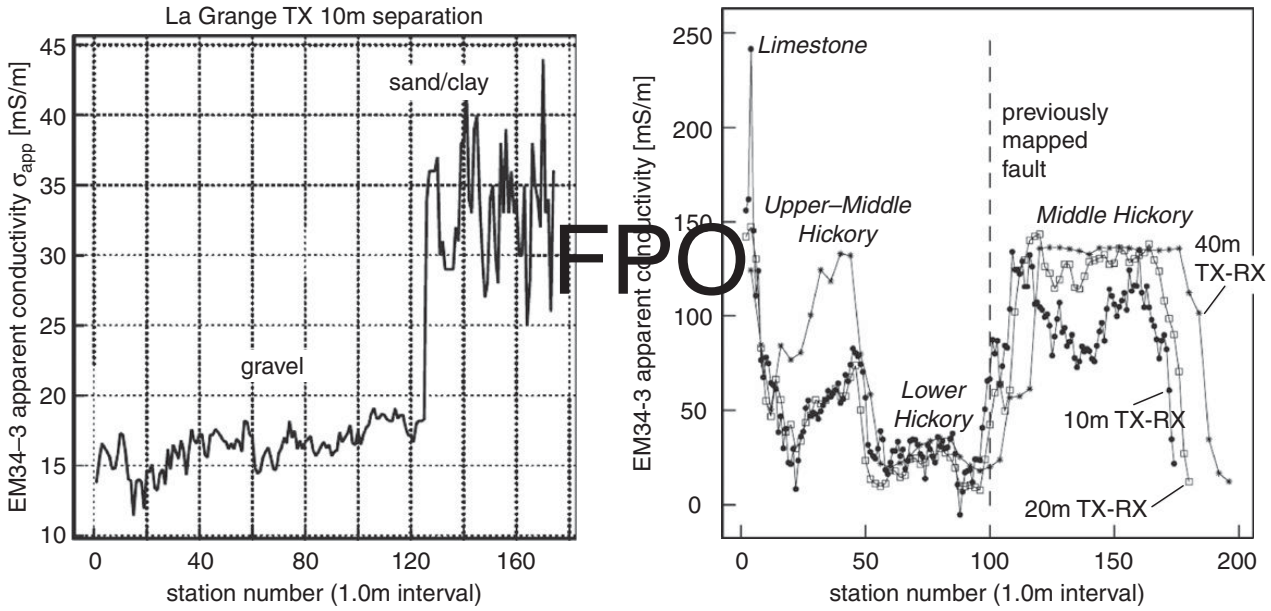

Figure 8.12 EM34 mapping of lateral geological discontinuities: (left) gravel quarry; (right) faulted Cambrian sandstone aquifer. After Everett and Meju (2005).

The observed lateral contrasts in apparent electrical conductivity are caused by lateral variations in sedimentary texture. For example, the location of a previously mapped, buried fault is shown by the dotted line. The variations in the EM34 responses between stations 20–50 can be explained in terms of spatial variations in the distribution of clays within the Hickory sandstone formation (Gorman *et al*., 1998).

8.6 Time-domain EM induction

A physical understanding of *transient* CSEM responses can be obtained by recognizing that the induction process is equivalent to the diffusion of an image of the transmitter (TX) loop into a conducting medium. The similarity of the equations governing electromagnetic induction and hydrodynamic vortex motion, first noticed by Helmholtz, leads directly to the association of the image current with a smoke ring (Lamb, 1945; p. 210). The latter is not "blown," as commonly thought, but instead moves by self-induction with a velocity that is generated by the smoke ring's own vorticity and described by the familiar Biot–Savart law (Arms and Hama, 1965). An electromagnetic smoke ring dissipates in a conducting medium much as the strength of a hydrodynamic eddy is attenuated by the viscosity of its host fluid (Taylor, 1958; pp. 96–101). The material property that dissipates the electromagnetic smoke ring is electrical conductivity.

The operating principles of an inductively coupled time-domain electromagnetic (TDEM) system are summarized as follows. A typical current waveform $I(t)$ consists of a slow rise to a steady value of I_0 followed by a rapid shut-off as exemplified by the linear ramp shown in Figure 8.13a. Passing such a disturbance through the TX loop generates a primary magnetic field that is in-phase with, and proportional to, the TX current. According to Faraday's law of induction, an impulsive electromotive force (emf) that scales with the negative time rate of change of the primary magnetic field is also generated. The emf drives electromagnetic eddy currents in the conductive Earth, notably in this case during the ramp-off interval, as shown in Figure 8.13b. After the ramp is terminated, the emf vanishes and the eddy currents start to decay via Ohmic dissipation of heat. A weak, secondary magnetic field is produced in proportion to the waning strength of the eddy currents. The receiver (RX) coil voltage measures the time rate of change of the decaying secondary magnetic field, Figure 8.13c. In many TDEM systems, RX voltage measurements are made during the TX off-time when the primary field is absent. The advantage of making off-time measurements is that the relatively weak secondary signal is not swamped by the much stronger primary signal. A good tutorial article on TDEM has been written by Nabighian and Macnae (1991).

During the ramp-off, the induced current assumes the shape of the horizontal projection, or shadow, of the TX loop onto the surface of the conducting ground. The sense of the circulating induced currents is such that the secondary magnetic field they create tends to maintain the total magnetic field at its original steady-on value prior to the TX ramp-off. In this case, therefore, the induced currents flow in the same direction as the TX current, i.e. opposing the TX current decrease that served as the emf source. The image current then

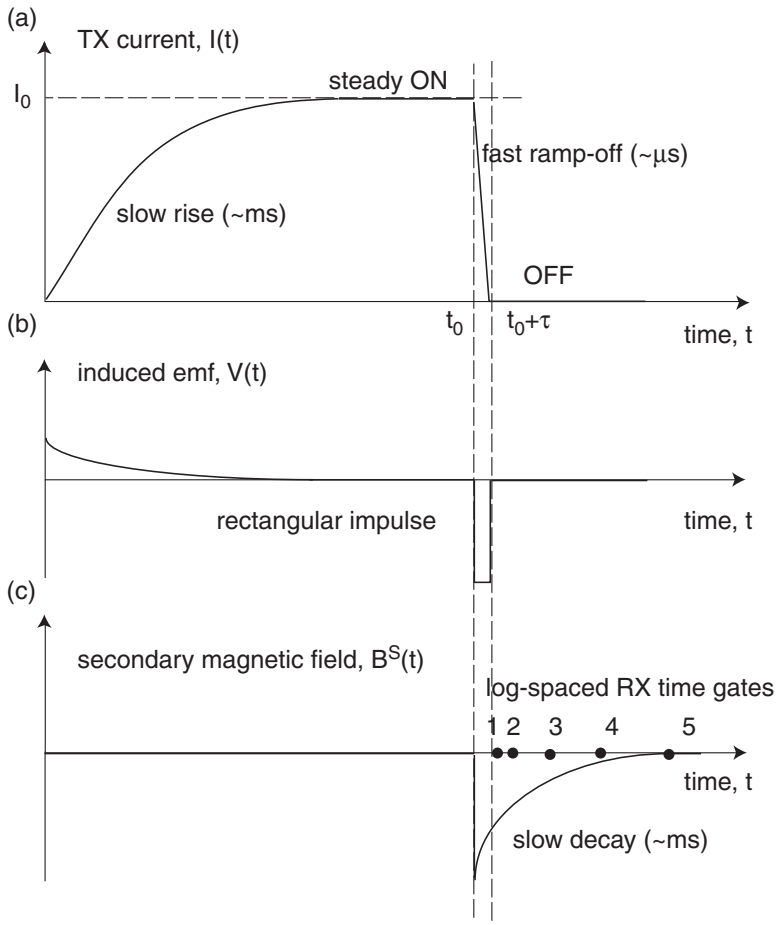

Figure 8.13 (a) A typical TX waveform $I(t)$ with slow rise and fast ramp-off; (b) induced emf $V(t)$ proportional to the time rate of change of the primary magnetic field; (c) the decaying secondary magnetic field $B^S(t)$ due to dissipation of currents induced in the ground.

diffuses downward and outward while diminishing in amplitude. A series of snapshots in Figure 8.14 of the secondary electric field intensity illustrates the transient diffusion of the electromagnetic smoke ring into a uniform halfspace.

In the widely used central-loop sounding method, the RX loop is placed at the center of the TX loop, while in TDEM offset-loop soundings the TX and RX loops are separated by some distance L. As indicated in Figure 8.15, at a fixed instant in time t, the vertical magnetic field $H_z(L)$ due to the underground smoke ring exhibits a sign change from positive to negative as distance L increases. In other words, the vertical magnetic field $H_z(t)$ changes sign from positive to negative as the smoke ring passes beneath a fixed measurement location. It should be clear to the reader that a central-loop measurement of the vertical magnetic field $H_z(t)$ does not exhibit such a sign change.

The "normal moveout" of the sign reversal with increasing TX–RX separation distance L is shown in Figure 8.16. The sharp cusps in the response curves mark the transition between positive and negative flux passing through a RX loop placed at distance L from the TX loop. These solutions correspond to the response of a uniform halfspace of $\sigma \sim 0.1$ S/m, as indicated in the figure legends. Note the late-time responses scale as a power law of

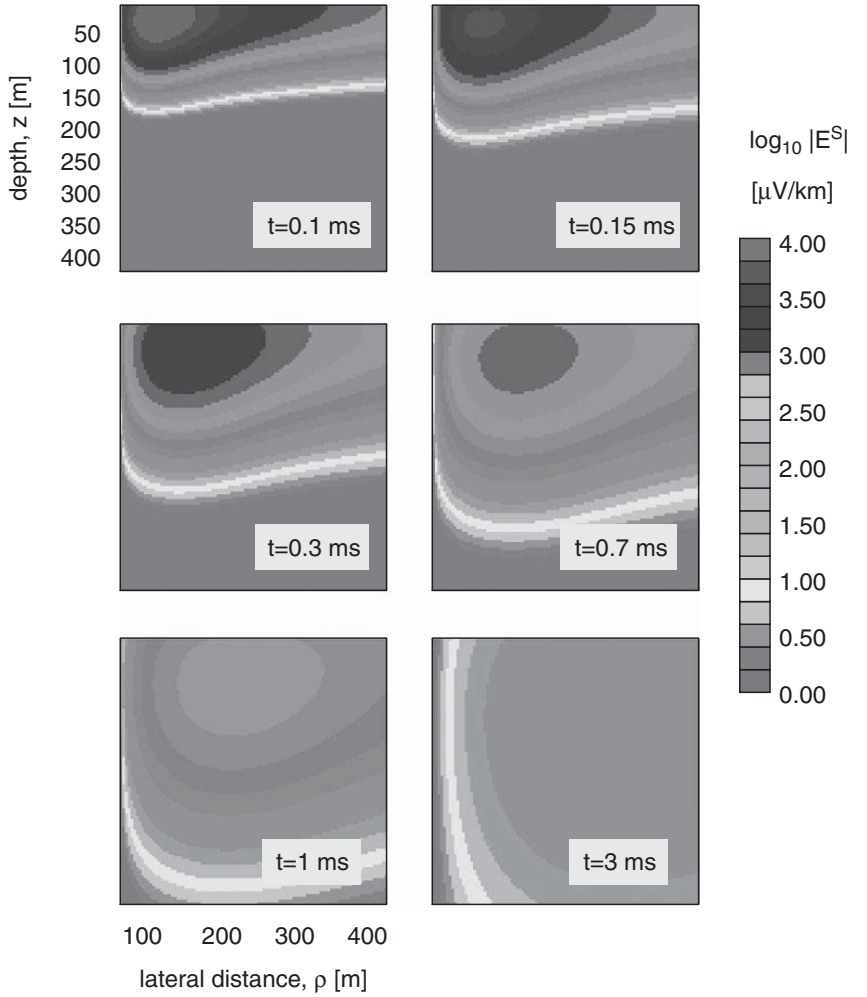

Figure 8.14 Transient smoke-ring diffusion into a uniformly conductive halfspace, $\sigma = 0.1$ S/m.

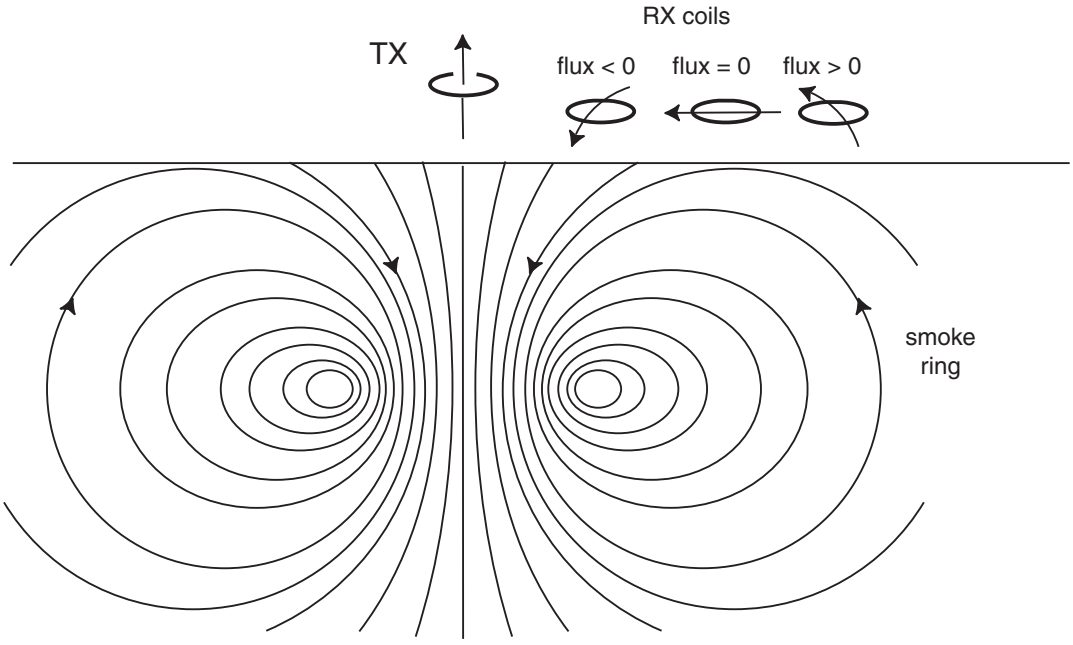

Figure 8.15 The changing sign of magnetic flux from the smoke ring as a function of TX–RX separation. After Nabighian and Macnae (1991).

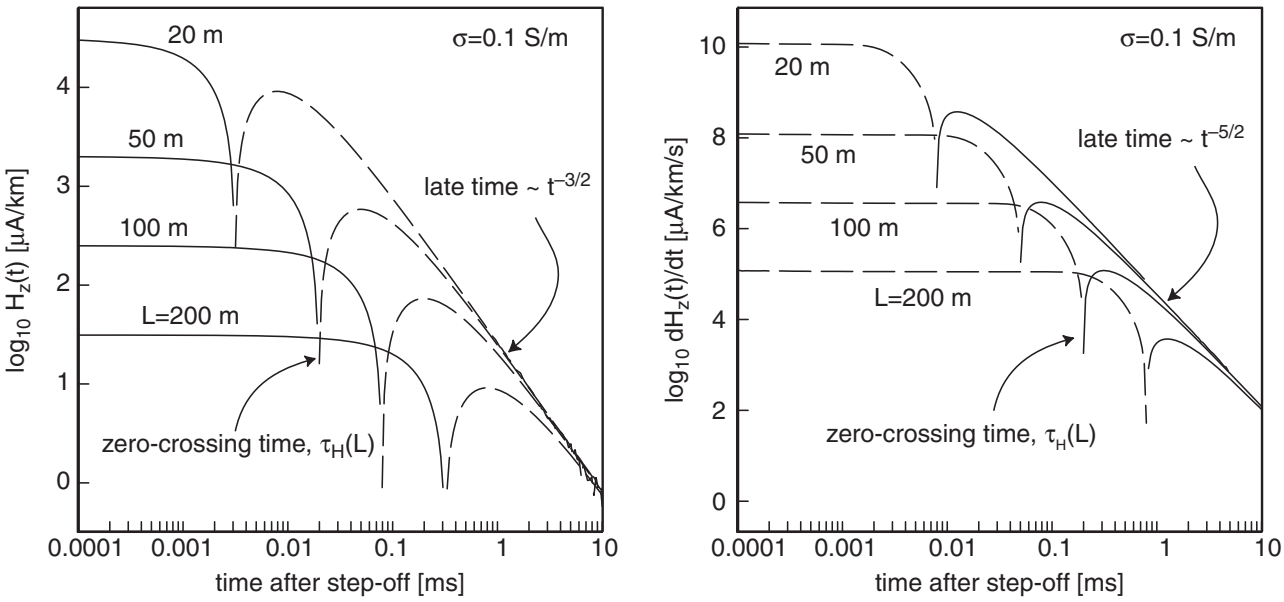

Figure 8.16 (Left) Transient step-off vertical magnetic-field response, horizontal loop source; (right) transient step-off RX voltage response, horizontal loop source.

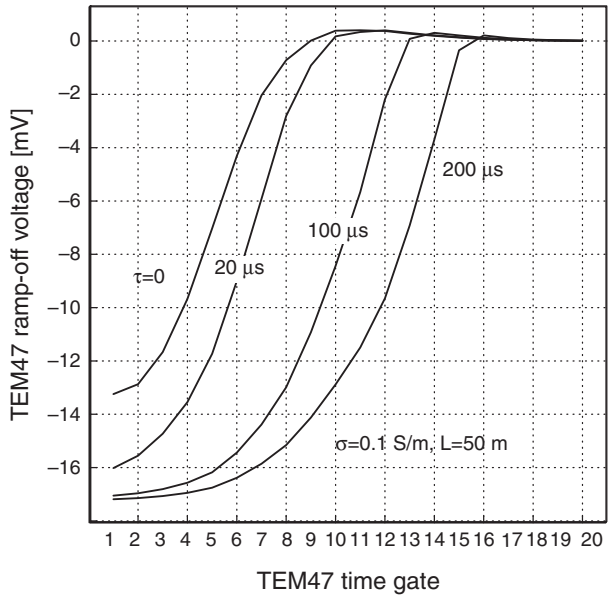

Figure 8.17 Effect of finite ramp-off time on TEM47 response.

the form $t^{-3/2}$ for the magnetic field and, since it is proportional to the time-derivative of the magnetic field, of the form $t^{-5/2}$ for the induction-coil response.

In the ideal TDEM case, step-off transients are analyzed. However, it is impractial in the field to abruptly switch off the current in a finite-sized loop due to self-inductance effects. Consequently, most systems are linearly ramped off over a brief time interval on the order of microseconds. The impact of using a finite TX ramp-off time on the TDEM response is shown in Figure 8.17. For fixed TX–RX separation L, an increase in the ramp-off time τ

serves to delay the response measured at the receiver. The curves in Figure 8.17 are simulated Geonics TEM47 (a popular commercial TDEM instrument) responses that have been computed by convolving the theoretical impulse reponse with a linear ramp-off function of width τ (Fitterman and Anderson, 1987). The curve labeled $\tau = 0$ is the ideal step-off response. The curves are plotted for the logarithmically-spaced times, after initiation of the ramp-off, at which the TEM47 system samples the response.

8.7 Finite-source excitation of a layered Earth

A classic problem of considerable practical importance in near-surface applied geophysics is to determine the electromagnetic response of a plane-layered Earth to finite-source excitation. There are well-known analytic solutions to the Maxwell equations available for finite-sized loops of horizontal and vertical orientation and horizontal grounded sources of finite length; while these are broadly scattered throughout the literature, many are derived in Ward and Hohmann (1989).

In this section we indicate some analytic frequency-domain solutions to a few problems of inductive or grounded-source sounding of a layered halfspace. For example, the electromagnetic response of a horizontal loop source of finite radius, like that shown in Figure 8.18, is derived in Morrison *et al*. (1969) and Ryu *et al*. (1970).

From the complete derivation given in Appendix D, the vertical magnetic field recorded by an RX coil placed on the surface $z = 0$ above a homogeneous ground is found to be

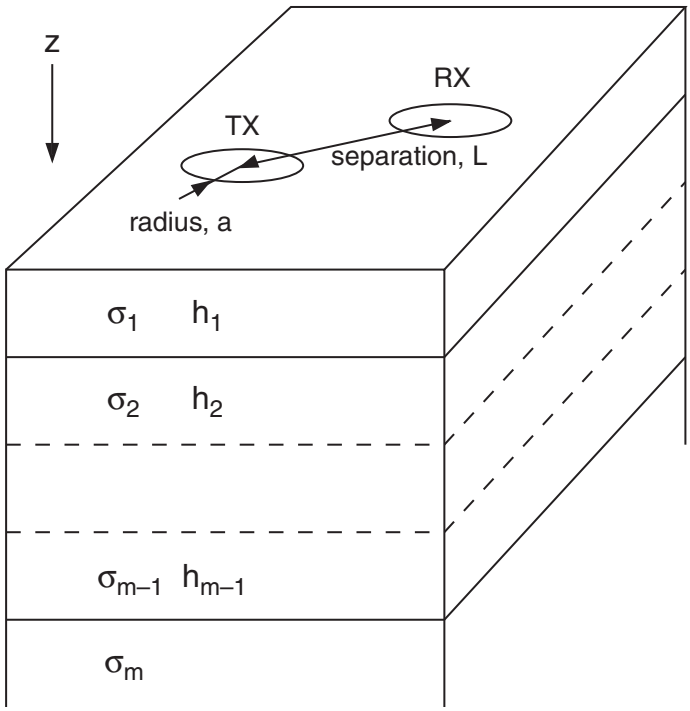

Figure 8.18 Horizontal TX and RX loops on a layered halfspace.

$$b_z(\rho) = \mu_0 Ia \int_0^\infty \frac{\lambda^2}{\lambda + i\gamma} J_1(\lambda a) J_0(\lambda \rho) d\lambda, \tag{8.29}$$

where the time-harmonic dependence has been suppressed and now ρ is the TX–RX coil separation. The TX loop radius is a, it carries current I, and J_0, J_1 are Bessel functions. The parameter $\gamma = \sqrt{\alpha^2 - \lambda^2} = \sqrt{-i\mu_0\sigma\omega - \lambda^2}$ has the dimensions of a wavenumber. A derivation of the solution for the m-layered Earth is left for the reader as an exercise at the end of the chapter.

In most if not all 1-D layered Earth problems, the electric and magnetic fields can be written as Hankel transforms, or integrals over Bessel functions. Various algorithms that can numerically evaluate Hankel tranforms in a fast and reliable manner are readily available. The numerical algorithms are based on convolution, digital filtering, or other specialized quadrature techniques (e.g. Anderson, 1979; Chave, 1983; Guptasarma and Singh, 1997). Transient layered-Earth responses are typically found by inverse Fourier or, occasionally, inverse Laplace transform of the corresponding frequency-domain responses.

The electromagnetic response of a vertical loop of small radius (treated as a horizontal magnetic dipole) over a layered Earth is solved by Dey and Ward (1970). This problem is more difficult to solve than the horizontal-loop problem since it does not possess azimuthal symmetry. Passalacqua (1983) solves the problem of a finite-length grounded horizontal electric dipole deployed over a layered Earth. Finally, Poddar (1983), using a reciprocity principle, develops the solution for a rectangular loop source deployed over a layered Earth. Finally, the article by Spies and Frischknecht (1991) contains a large number of calculated layered-Earth response curves for various combinations of transmitter and receiver coils.

8.8 Plane-wave excitation methods: VLF, RMT, CSMT

To this point, we have been considering electromagnetic geophysical methods that utilize a controlled source of finite extent, most commonly a loop source. The measurements are assumed to be made close enough to the source that the spatial distribution of the primary transmitted field exhibits some curvature. Another class of EM methods has been developed that is based on plane-wave excitation from distant sources. The classical plane-wave method for deep-crustal and upper-mantle exploration is the magnetotelluric (MT) method (Simpson and Bahr, 2005; Chave and Jones, 2012), which is based on excitation by long-period ($f \sim 0.1$ mHz to 300 Hz) geomagnetic disturbances originating principally in the ionosphere at an altitude $h\sim$ 110 km, with skin depths $\delta \sim 300$ m to 50 km. The adaptation of plane-wave methods for near-surface investigations has been reviewed by Tezkan (1999). A number of such methods exists; herein, we focus brief attention on the relevant aspects of the very-low-frequency (VLF), VLF–resistivity (VLF–R), radiomagnetotelluric (RMT), and controlled-source magnetotelluric (CSMT) methods along with a few of their variants.

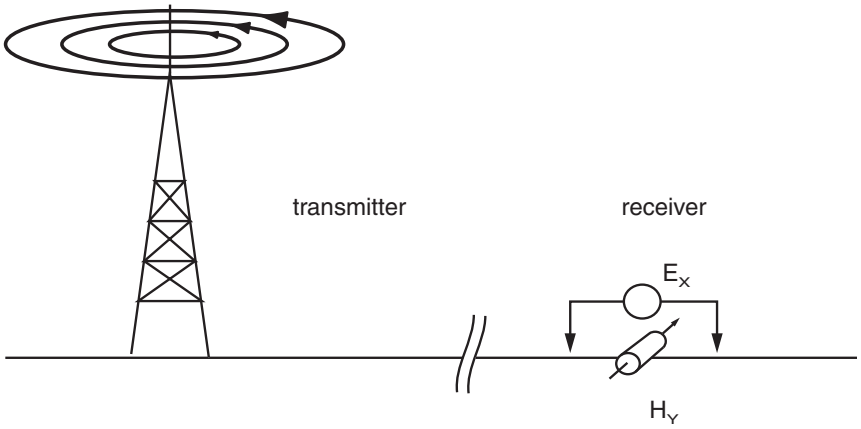

Figure 8.19 The VLF–R method is based on measurements of E_x and H_y signals due to transmissions from a distant radio antenna over variably conductive ground.

The VLF and VLF–R methods take advantage of the electromagnetic field generated by a distant, powerful radio transmitter (the VLF–R configuration is shown in Figure 8.19). Maps showing the locations and global coverage of a number of such transmitters are provided by McNeill and Labson (1991). The carrier signal is typically in the 15–30 kHz frequency range. At great distances from a transmitter, which acts as a vertical electric dipole, the primary field can be approximated as a cylindrical plane wave with non-zero components (E_z, H_ϕ). The transmitted plane wave propagates almost horizontally, arriving to a remote receiver location at grazing incidence.

The small angle of incidence, coupled with the large constrast in electrical conductivity between the air and the ground, results in a transmitted plane wave that propagates essentially downward into the conductive Earth. The principal effect, at the surface, of this vertically attenuating plane wave is to generate local, secondary field components (E_x, H_z) whose amplitude and phase depends on the terrain conductivity (McNeill and Labson, 1991), and where the $\hat{\mathbf{X}}$ direction is parallel to a line drawn between the transmitter and a receiver deployed at the surface.

In the classical VLF technique (Parasnis, 1997; Sharma, 1997), a single RX coil is tuned to the TX frequency, aligned to the transmitter azimuth, and then rotated up and down until a minimum signal is found. The TE mode is excited if the RX station is located such that the incoming VLF wave propagates along the predominant geological strike direction. If that is the case, then the tilt angle θ at which the minimum signal is found is a measure of the in-phase (real) component of H_z, denoted by $\mathrm{Re}(H_z)$, normalized by the strength of the primary magnetic field H_ϕ,

$$\theta \sim \frac{\mathrm{Re}(H_z)}{|H_\phi|}. \tag{8.32}$$

A distinct tilt-angle anomaly is generated by a lateral discontinuity in terrain conductivity. The tilt angle changes sign over a tabular conductor, as shown in Figure 8.20. A TM mode of excitation is also possible if the transmitter direction is perpendicular to the predominant geological strike. Generally, VLF methods are well suited to detect tabular features such as water-bearing fractures or faults. A number of field examples are presented in McNeill and

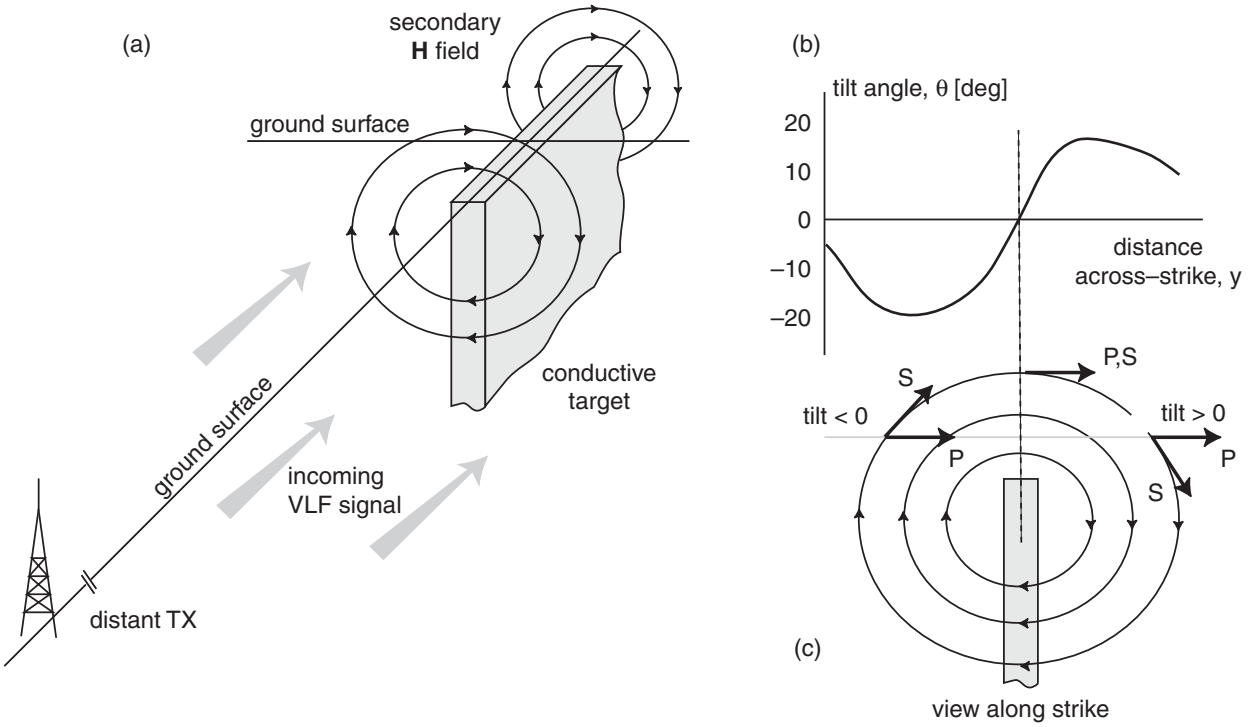

Figure 8.20 VLF (TE mode) exploration of a tabular conductor: (a) the interaction between the incoming plane wave from a distant transmitter and a tabular conductor generates a secondary magnetic field, as shown; (b) the tilt angle as a function of location across the strike of the conductor; (c) explanation of the tilt-angle curve, P = primary magnetic field, S = secondary magnetic field.

Labson (1991). A more recent case study using VLF data to detect faults in a granite quarry is found in Gurer *et al*. (2008).

The quantity measured in the VLF–R method is the ratio of *horizontal* field components E_x and H_y, as suggested in Figure 8.19. The electrodes are normally oriented in the direction of the transmitter. An apparent resistivity ρ_a and phase φ at the observed frequency ω is defined as

$$\rho_a = \frac{1}{\omega\mu_0}\left|\frac{E_x}{H_y}\right|^2; \tag{8.33}$$

$$\varphi = \tan^{-1}\left[\frac{\mathrm{Im}(E_x/H_y)}{\mathrm{Re}(E_x/H_y)}\right]. \tag{8.34}$$

The quantities (ρ_a, φ) are affected by lateral variations in the subsurface conductivity structure and hence contain information about the geology in the intervening region between the transmitter and receiver locations (Beamish, 2000). However, VLF and VLF–R techniques offer poor depth resolution since measurements are made at only one frequency.

Radiomagnetotellurics (RMT) is essentially an extension of the VLF–R method to multiple and higher frequencies, toward the 100 kHz to 1 MHz range (Tezkan, 1999). The RMT method uses simultaneously the transmissions from a number of radio sources

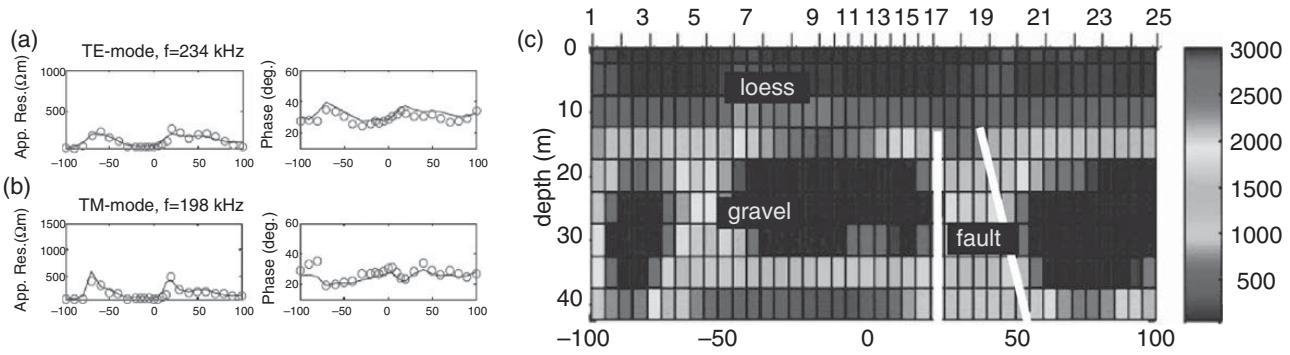

Figure 8.21 RMT survey results from Cologne, Germany: (a) TE-mode apparent resistivity and phase at 234 kHz; (b) TM-mode apparent resistivity and phase at 198 kHz. Blue lines are observed data, while red circles are computed from the resistivity model shown at right; (c) 2-D RMT smooth inversion result. The color bar indicates resistivity ρ [Ωm]. The plot ordinates in all cases is RX location [m]. After Candansayar and Tezkan (2008).

distributed over a range of azimuths relative to the survey area. The method is popular in Europe due to the abundance of transmitters and is being used increasingly there and elsewhere for engineering and environmental applications since the skin depths are small, $\delta \sim 5$–10 m. Measurements are made of ratios of horizontal field components and these are converted into apparent resistivity and phase, as in Equations (8.33) and (8.34). The use of multiple frequencies permits the determination of subsurface electrical conductivity profiles with depth. Data from along a profile of measurement sites can be inverted for 2-D subsurface conductivity structure using standard MT inversion routines (e.g. Simpson and Bahr, 2005).

An RMT survey conducted by Candansayar and Tezkan (2008) crossed a near-surface fault outside the city of Cologne, Germany. The geology at the site consists of a conductive wind-blown silt (loess) layer of ~ 15–20 m overlying a resistive gravel unit. The gravel is cut by a steeply dipping, conductive fault of thickness ~ 12–15 m. A total of 25 radio stations spanning the frequency range 10–240 kHz served as the plane-wave sources. The radio stations were located at different azimuths, thus providing both TE- and TM-mode excitation. RMT apparent resistivities and phases were acquired every 5–10 m along a single profile. Representative RMT data are shown in Figure 8.21a, b. The complete dataset was inverted to obtain the 2-D resistivity distribution $\rho(x, z)$ shown in Figure 8.21c. A non-linear, smooth least-squares inversion approach was used; such methods are discussed in Chapter 12. The inversion result shows the moderately conductive fault cutting across the resistive gravel unit.

The controlled-source magnetotelluric (CSMT) methods (Goldstein and Strangway, 1975; Zonge and Hughes, 1991) are similar to the MT and RMT methods except that the source consists of one or more remote grounded dipoles or a large horizontal loop source instead of, respectively, natural ionospheric disturbances or distant radio transmitters (Figure 8.22). The main advantage of a CSMT method is that the geophysicist can control important parameters such as the orientation, location, length/radius, and moment of the transmitter, and the selection of frequencies to be used. A major drawback is that a long, powerful grounded dipole or large horizontal loop can become unwieldy to deploy in the field. As in the RMT method, measurements at selected receiver locations are made of TE-

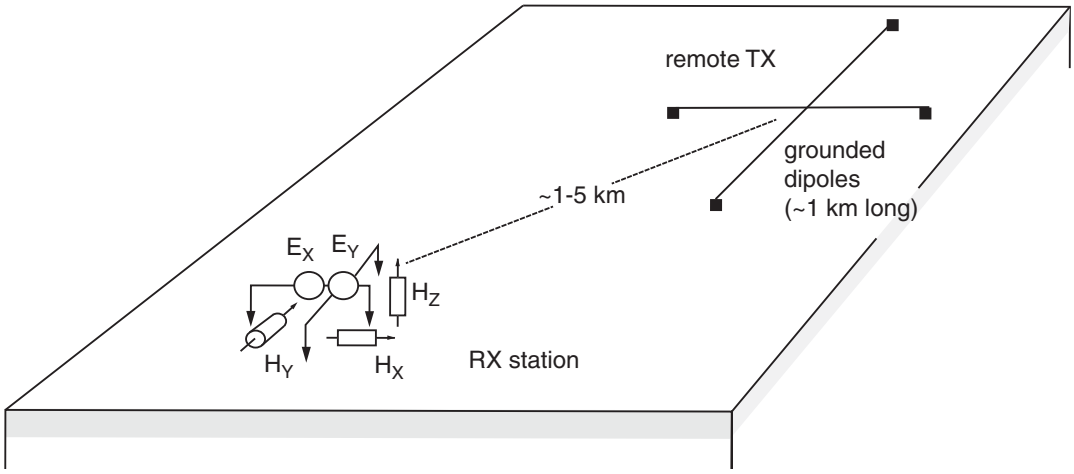

Figure 8.22 A typical tensor CSMT exploration setup with orthogonal TX grounded dipoles and a RX station consisting of surface measurements of 5 EM field components (E_x, E_y, H_x, H_y, H_z).

mode and TM-mode surface impedances which are then converted into apparent resistivity and phase estimates.

In CSMT experiments, the electric and magnetic field receivers should be placed at a sufficient distance from the dipole or loop transmitter such that plane-wave analysis can be used to interpret the data. The plane-wave approximation generally requires that the TX–RX separation distance is ~ 4–20 skin depths (Goldstein and Strangway, 1975; Wannamaker, 1997) with the latter value prevailing if the geology consists of conductive sediments over resistive basement. A wide frequency range has been used for CSMT measurements, between f~ 1 Hz–20 kHz, depending on the required depth of signal penetration.

Ismail and Pedersen (2011) combined multi-component (tensor) CSMT (1–12 kHz) and RMT (14–250 kHz) techniques to map the resistivity structure of fracture zones located at ~ 150 m depth within Precambrian crystalline bedrock of Sweden. The RMT data imaged the upper conductive clay layer while the CSMT data successfully probed deeper into the bedrock. A focus of the investigation concerned the applicability of plane-wave, or far-field, techniques since the controlled loop source was located only ~ 300–600 m from the RX profiles. It was found that near-field effects were prominent especially in the low-frequency TM-mode phase responses. These data should be downweighted, or not used at all, if a conventional CSMT 2-D inversion based on a plane-wave source assumption is used. In general, a full 2.5-D (i.e. 3-D-source excitation of 2-D Earth structure) inversion is recommended to interpret data that are strongly influenced by near-field effects (see Figure 8.23).

8.9 Airborne electromagnetics

The airborne electromagnetic (AEM) method has been used for decades in the mining industry as a primary geophysical tool to locate and delineate economic mineral deposits. There have been significant recent developments in near-surface AEM applications, as reviewed by

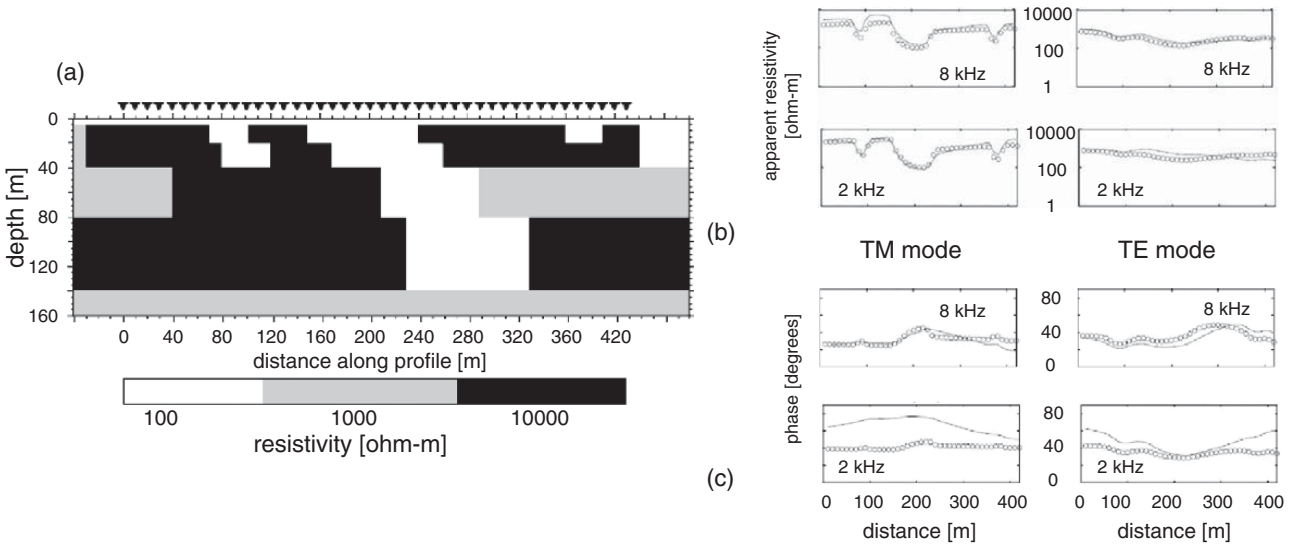

Figure 8.23 Test of the CSMT plane-wave assumption. The 2-D resistivity model in (a) is excited by TE- and TM-mode plane-wave sources and a loop source located 300 m along strike. Computed responses at 2 and 8 kHz, in the form of apparent-resistivity and phase profiles, are shown in (b) and (c), respectively. The circles show the plane-wave responses while the solid lines show the 2.5-D controlled-source responses. As mentioned in the text, the most significant differences appear in the low-frequency TM-mode phase responses. After Ismail and Pedersen (2011).

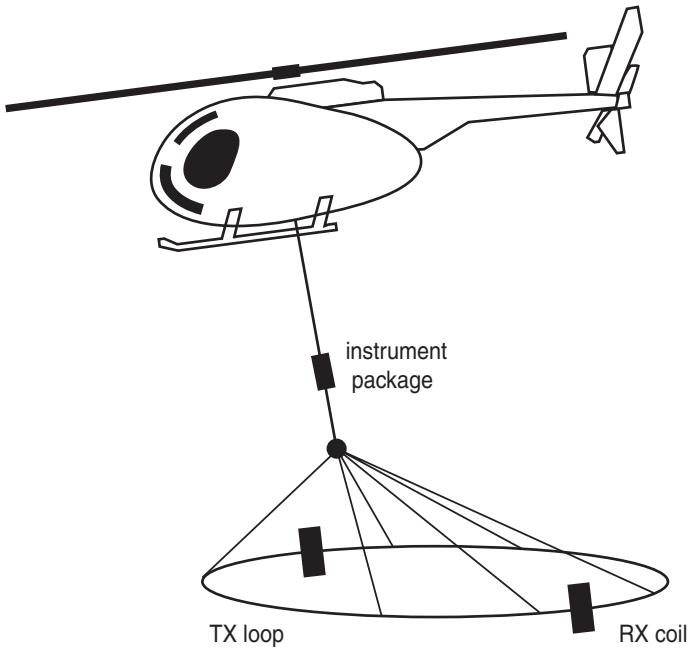

Figure 8.24 A helicopter AEM system.

Auken *et al*. (2006). In most AEM systems a transmitter loop is either mounted on or towed beneath a helicopter or a fixed-wing aircraft and at least one receiver coil is either mounted on or towed behind or beneath the aircraft along with an instrument package sometimes called the bird. A simplified illustration of an AEM system is shown in Figure 8.24.

The operating principles of an AEM system are essentially the same as those of ground-based loop–loop electromagnetic systems, described earlier. Both frequency-domain and time-domain systems are in present use. AEM data processing must take into account a number of important sources of noise including in-flight variations of the altitude and tilt of the mechanical assembly that supports the TX loop and RX coils. The processed data are then usually interpreted based on 1-D layered-Earth forward modeling combined with some type of stable, regularized least-squares inversion (see Chapter 12). In the widely used spatially constrained inversion (SCI) method (Viezzoli *et al*., 2008), for example, smoothness constraints are enforced that prevent the introduction of flight-line artefacts and other unphysical, sharp lateral changes in the reconstructed subsurface electrical conductivity structure. Examples of the use of AEM systems for hydrogeological investigations are provided at the beginning and the end of this chapter.

8.10 EM responses of rough geological media

The EM method provides valuable non-invasive information about the subsurface electrical-conductivity distribution for a range of applications in hydrology, such as groundwater-resource evaluation, contaminant-transport investigation, and the characterization of aquifer heterogeneity. While traditional approaches treat electrical conductivity as a piecewise smooth medium, perhaps a more efficient and realistic description of conductivity can be attained if the inherent roughness of the underlying geological medium is explicitly recognized. The spatial roughness of fractured rocks, and the attendant implications for subsurface fluid transport, has been carefully analyzed by hydrologists (e.g. Painter, 1996; Bonnet *et al*., 2001; Berkowitz and Sher, 2005). Rough geology is characterized by patterns of spatial heterogeneity that vary over a wide range of length scales.

To explore the electromagnetic response of such a medium, EM-34 measurements were made on the campus of Texas A&M University in Brazos County, as reported in Everett and Weiss (2002). The geological section consists of floodplain alluvium, mainly interbedded sands, silts, and clays with occasional coarse sand and gravel lenses and paleochannels. An azimuthal apparent-conductivity profile $\sigma_a(\theta)$ was acquired (Figure 8.25a) by fixing the position of the TX loop and moving the RX loop in a complete circle around the TX loop at fixed radius 40 m. The apparent conductivity was read at 512 RX azimuths, so that station spacing is 0.5 m. The data, shown in Figure 8.25a, are highly irregular. The traditional interpretation of the EM response as being caused by a piecewise smoothly varying conductivity structure superposed with random, uncorrelated noise is not supported this dataset. Instead, the responses are examples of fractional Brownian motion (fBm), a class of non-stationary signals that describe self-similar processes with long-range correlations (Mandelbrot and van Ness, 1968). An fBm signal is further characterized by stationary increments.

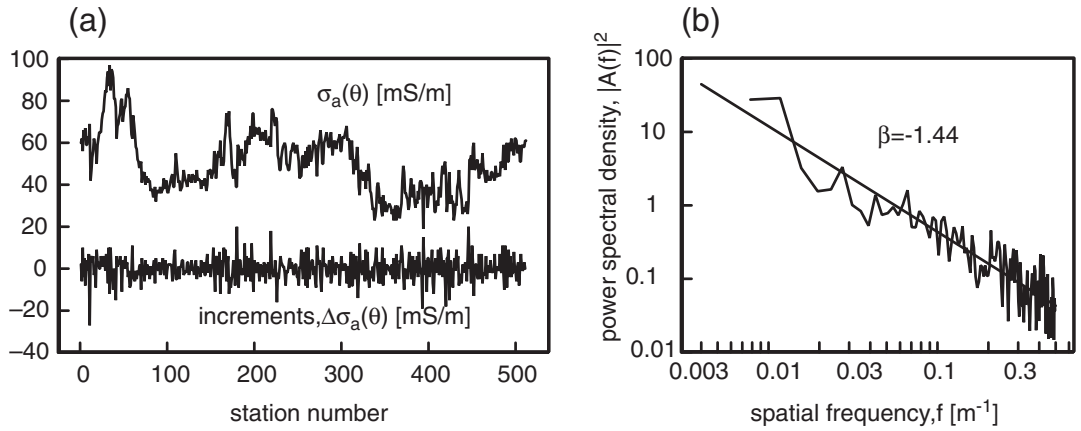

Figure 8.25 (a) EM34 apparent-conductivity measurements from the Brazos River (TX) floodplain; (b) Power spectrum of the apparent-conductivity data. After Everett and Weiss (2002).

While the response σ_a in Figure 8.25a is clearly non-stationary, i.e. the mean value fluctuates along the profile, the increments $\Delta\sigma_a(\theta)$, or differences between consecutive data points, appear to be stationary with nearly zero mean over the entire profile. Thus, the apparent-conductivity profile suggests a fractal interpretation of electromagnetic induction in the Earth. This suggestion is further supported by the power spectral density (PSD) function. The PSD of the EM34 σ_a profile is shown in Figure 8.25b. A power-law of the form $|A(f)|^2 \sim f^{\beta}$ over 2.5 decades in the spatial wavenumber f is evident. The slope is $\beta = -1.44 \pm 0.06$. A value of $|\beta| > 1.0$ indicates a non-Gaussian fractal signal (Eke *et al.*, 2000). For comparison, the PSD of the increments $\Delta\sigma_a$ has slope $\beta = 0.43 \pm 0.06$ which indicates that the increments are a realization of fractional Gaussian noise, that is, a stationary signal without significant long-range correlation. A pure white-noise process would have a PSD slope of exactly $\beta = 0$.

The foregoing analysis shows that spatial variations in the EM response due to rough geological structure may be characterized by a power-law wavenumber spectrum. The presence of a buried man-made conductive target, with a regular geometry, should generate a departure from a power-law spectrum. This was shown by Benavides and Everett (2005). In their experiment, EM31 apparent-conductivity readings were acquired along a profile of length 152.0 m with 1.0 m station spacing. A buried metal drainage culvert was located where the profile crossed a gravel road. The power spectra of the EM31 data are shown in Figure 8.26. Analyzing the data from the first part of the profile, which contains only the background geology but not the culvert, yields the familiar power-law spectrum (gray). The PSD slope is $\beta = 1.417$, corresponding to an fBm signal. The spectrum shown in black is from the entire profile, including the culvert. It shows anomalously high power in the wavenumber range $f \sim$ 10–40 m^{-1}. This anomalous peak in the power spectrum is indicative of a compact, deterministic signal overlying the purely geologic fBm signal.

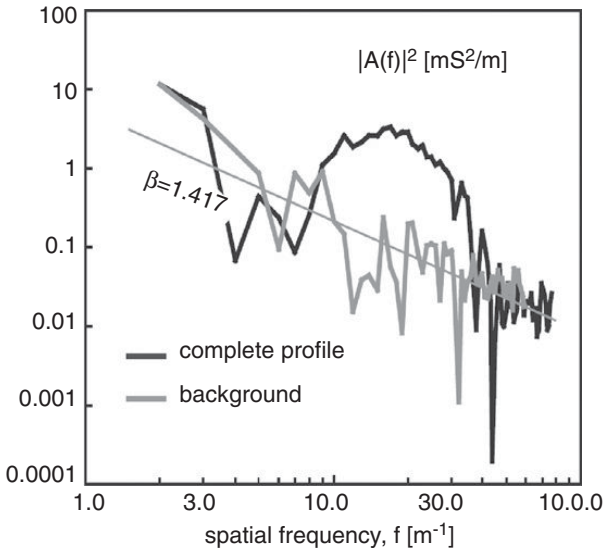

Figure 8.26 The departure from a power-law spectrum due to a buried conductive target. After Benavides and Everett (2005).

8.11 Anisotropy

Near-surface geophysicists now widely recognize that geological formations, as a rule, are electrically anisotropic. Most studies of electrical anisotropy for near-surface (i.e. depths $<$ 100 m) geophysical applications are based on azimuthal DC resistivity methods, as described earlier in Chapter 4. The EM method provides an alternative probe of anisotropic formations that includes the option of using an inductive or a grounded source. The variation of electrical anisotropy with depth can also be explored by using multiple frequencies or else a transient excitation.

In genaral, a minimum of two scalar parameters is required to characterize electrical anisotropy. These parameters may be termed the along-strike conductivity $\sigma_{||}$ and the across-strike anisotropy $\sigma_{\perp}$. The strike of the anisotropy is then the direction in which the conductivity is different from the isotropic conductivities of the other two directions. A familiar example is the interbedding of sediments, described by an electrical conductivity tensor of the form

$$\sigma = \text{diag}(\sigma_h, \sigma_h, \sigma_v), \tag{8.35}$$

in which the vertical conductivity σ_v differs from the isotropic horizontal conductivity σ_h. The strike of the anisotropy in that case is vertical. Any medium that has two distinct conductivities can be characterized by a *uniaxial* tensor. The reader should recall that the various geological realizations of a uniaxal conductivity tensor are illustrated in Figure 4.12. A *triaxial* conductivity tensor is more general; it is one in which the electrical conductivity is different in all three principal directions, that is $\sigma = \text{diag}(\sigma_x, \sigma_y, \sigma_z)$.

We restrict our attention in this section to horizontal anisotropy for which the electrical conductivity tensor is uniaxial and has the form

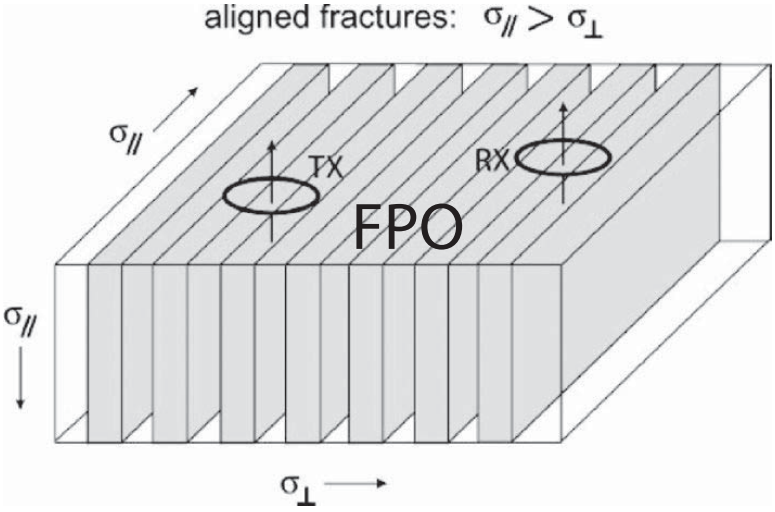

Figure 8.27 Loop–loop electromagnetic sounding over a uniform uniaxial conducting halfspace. After al-Garni and Everett (2003).

$$\sigma = \text{diag}(\sigma_{\perp}, \sigma_{||}, \sigma_{||}), \tag{8.36}$$

such that the strike is horizontal; specifically, it is in the $\hat{\mathbf{X}}$ direction. The conductivities in the two across-strike directions, $\hat{\mathbf{Y}}$ and $\hat{\mathbf{Z}}$, are identical. In an early study of such a horizontally anisotropic medium, Le Masne and Vasseur (1981) explored the frequency-domain electromagnetic response of a limestone formation pervaded by parallel vertical fractures. Yu and Edwards (1992) later derived theoretical CSEM responses of uniaxial media characterized by horizontal anisotopy.

Al-Garni and Everett (2003) studied the loop–loop frequency-domain response of an idealized set of vertical fractures for which $\sigma_{||} > \sigma_{\perp}$ (see Figure 8.27) and they found an electromagnetic paradox of anisotropy in which apparent conductivity σ_a, as defined by Equation (8.27), actually reads higher when the TX and RX loops are aligned across the strike of the anisotropy than when they are aligned along the strike. The paradox is resolved by recognizing that the electromagnetic response is not controlled by the conductivity aligned with TX–RX azimuth, but rather by the conductivity in the direction of the induced current flow beneath the RX loop.

The steeply dipping, weathered, foliated Packsaddle schist formation of the Llano Uplift in central Texas provided the ideal conditions for a field-scale azimuthal TDEM experiment (Collins *et al*., 2006) to detect horizontal anisotropy. The clay weathering products aligned with the foliations determine the most conductive direction. TEM47 voltage readings were made with a TX loop of 5 m radius held fixed at a central location while the RX coil was moved in a circular path, maintaining a constant TX–RX offset of 40 m. The observed TEM47 responses (Figure 8.28, left) vary with the TX–RX azimuth in the characteristic two-lobed pattern that is predicted by anisotropic forward modeling (Figure 8.28, right). The longer of the two principal axes is aligned at azimuth 146°, precisely parallel to the observed strike direction of the foliations. Isotropic forward modeling predicts that the early-time voltage (the first few time gates) should read higher

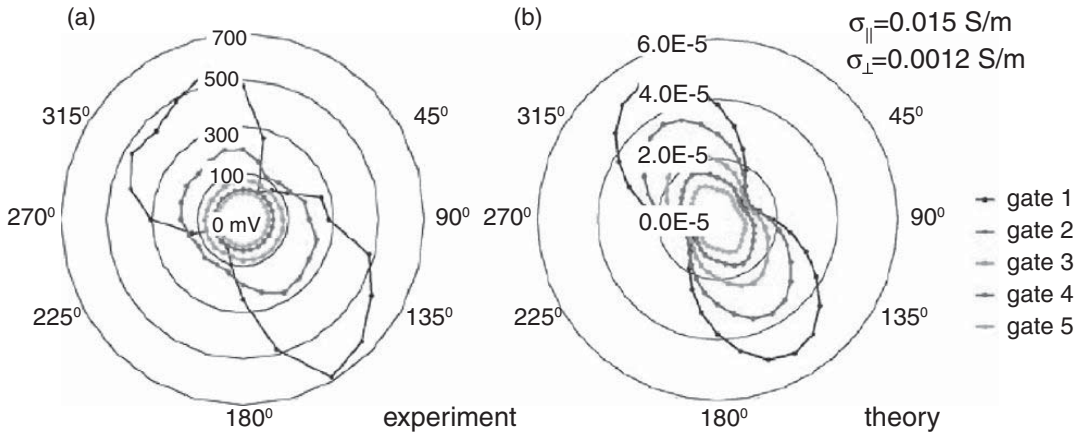

Figure 8.28 (Left) Azimuthal TEM47 voltage readings (first five time gates) over Packsaddle schist, central Texas; (right) calculated response [mV] of the horizontal anisotropic halfspace with $(\sigma_\perp, \sigma)$, as shown, with strike direction 146°. After Collins *et al*, (2006).

in a resistive medium than in a conductive medium. Naively, it would then hold that the longer principal axis should point in the most resistive direction. However, the paradox of anisotropic responses (al-Garni and Everett, 2003) predicts that the longer axis actually points in the most conductive direction, as observed in the field experiment. The two conductivities found by trial-and-error fit of the theoretical response to the observations are $\sigma_{||} = 0.015$ S/m and $\sigma_\perp = 0.0012$ S/m, which represent reasonable values for resistive metamorphic rocks. Moreover, the presence of the weathering products raises the bulk formation conductivity by more than order of magnitude in the foliation direction.

8.12 Illustrated case histories

Example. Arsenic contamination in Bangladesh.

This case study is an investigation into arsenic concentrations in Bangladesh by Aziz *et al*. (2008). It is well established that groundwater pumped from wells across the Bengal Basin often contains a hazardous (defined herein as > 50 μg/L) level of arsenic. The source of the arsenic is difficult to ascertain in view of the strongly heterogeneous fluvio-deltaic geology of the region. A 25-km^2 survey area was chosen in which ~ 5000 arsenic concentration values from shallow (< 22 m) Holocene aquifers were available.

Loop–loop frequency-domain electromagnetic data were then acquired to discriminate subsurface zones of clays and sands in an attempt to better understand the observed spatial variability of the arsenic concentration data. About 18 500 σ_a readings were made at ~ 4–8-m station spacing along a number of transects, typically 100 m–1 km in length, distributed across the survey area. A spatially continuous σ_a map was constructed by kriging

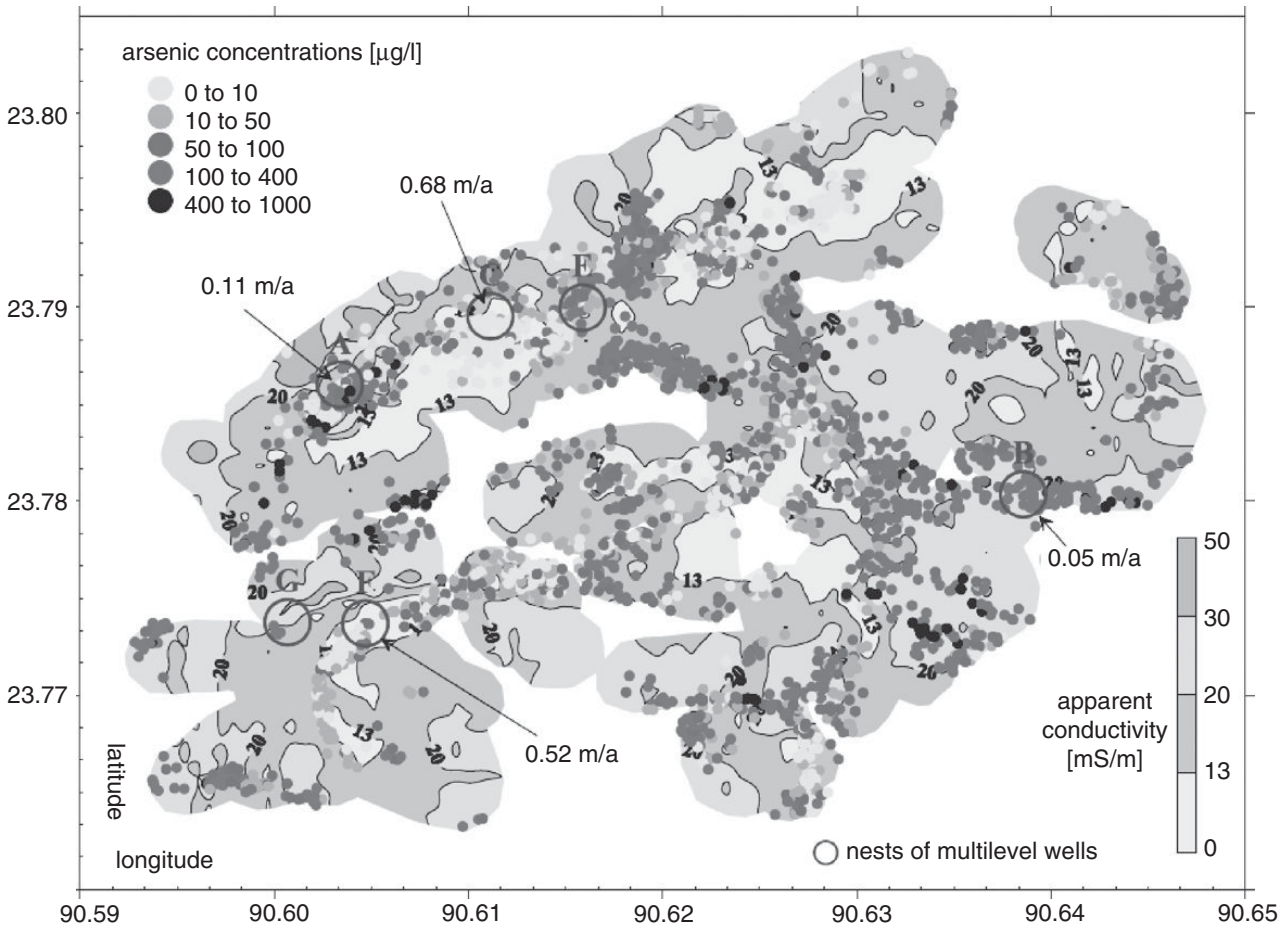

Figure 8.29 A spatially continuous kriged map of EM34 apparent-conductivity readings, along with arsenic concentration data from shallow wells, Bengal Basin. After Aziz *et al*. (2008).

(Figure 8.29). It is found that 73% of the wells show non-hazardous arsenic levels in the areas of low $\sigma_a < 10$ mS/m values, which are presumably sand-dominated regions. However, only 36% of the wells show non-hazardous arsenic levels in the high $\sigma_a > 10$ mS/m, clay-dominated regions. The σ_a values were also found to correlate with the depth gradient of arsenic concentration within a well. Overall, the findings suggest that the clay-dominated areas are at higher risk, since groundwater recharge percolating downward through sandy soils tends to prevent arsenic concentrations from rising to hazardous levels.

Example. CSMT at a radioactive waste disposal site.

The CSMT method in the audio frequency range (sometimes termed the CSAMT method) was used by Unsworth *et al*. (2000) to characterize the subsurface hydrological conditions beneath a proposed radioactive waste-disposal site at the Sellafield nuclear facility located

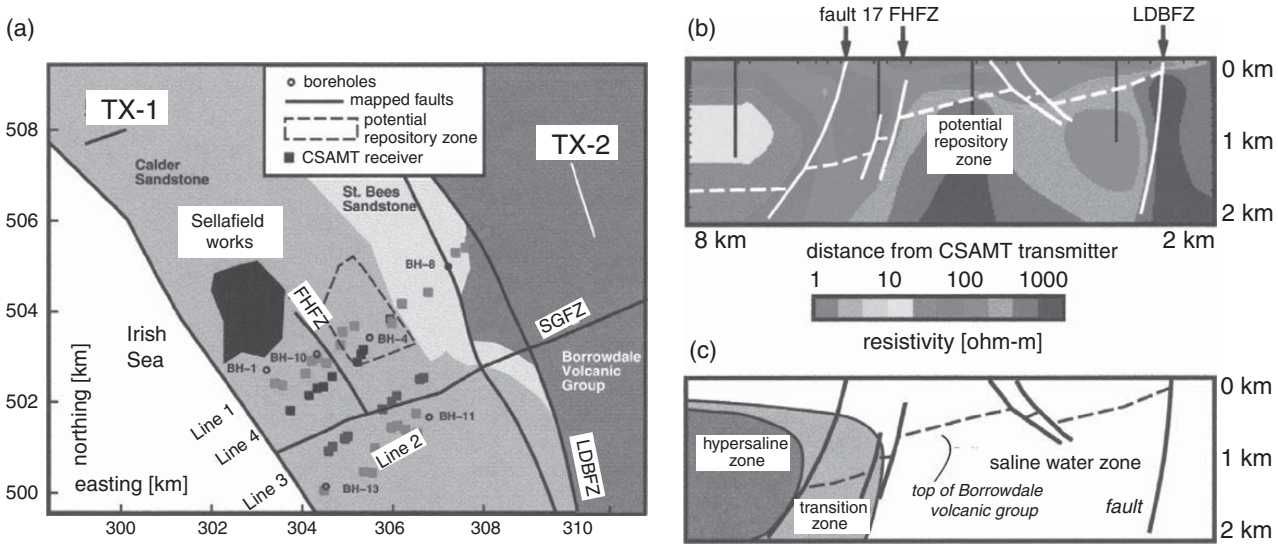

Figure 8.30 CSMT at the Sellafield (UK) nuclear facility: (a) layout of TX grounded dipoles and RX locations with respect to mapped faults and the power plant; (b) 2-D inversion result from Line 1; (c) hydrogeological interpretation. After Unsworth *et al*. (2000).

in coastal northwest England. The CSMT data were affected by intense cultural noise due to the infrastructure associated with the power plant. Nevertheless, the apparent resistivity and phase responses were found to be interpretable in terms of a 2-D resistivity section, with strike direction parallel to the coast. The two orthogonal, grounded dipole transmitters TX-1 and TX-2 (frequency range: 1 Hz–4 kHz) are shown in Figure 8.30a, along with the four CSMT RX profiles. The inverted resistivity model for Line 1, which crosses the proposed repository zone, is shown in Figure 8.30b. Known fault locations are overlain for reference. A hydrogeological interpretation of the resistivity section is shown in Figure 8.30c. The low-resistivity zone (yellow region) is caused by hypersaline groundwater associated with the Irish Sea extending ~ 1 km inland. Groundwater modeling suggests that the brines are likely to remain to the west of the proposed nuclear waste repository but, over geologic time, the site may be negatively impacted by migrating hypersaline waters.

Example. Airborne hydrogeophysics.

A helicopter transient AEM survey with ~ 300 m penetration depth was carried out by Auken *et al*. (2009) over a 190 km^2 area of Santa Cruz volcanic island in the Galapagos archipelago (Figure 8.31). The island has few freshwater resources; a fast-growing population; and unique, pristine ecosystems. Very little, however, is known about the hydrogeology. The acquisition of geophysical data improves this understanding and assists in the development of effective water-resource management strategies. The main exploration target is conductive zones perhaps indicative of water or clay confining layers that are located within the resistive ($> 1000\ \Omega$ m) volcanic terrain. A 3-D spatially constrained

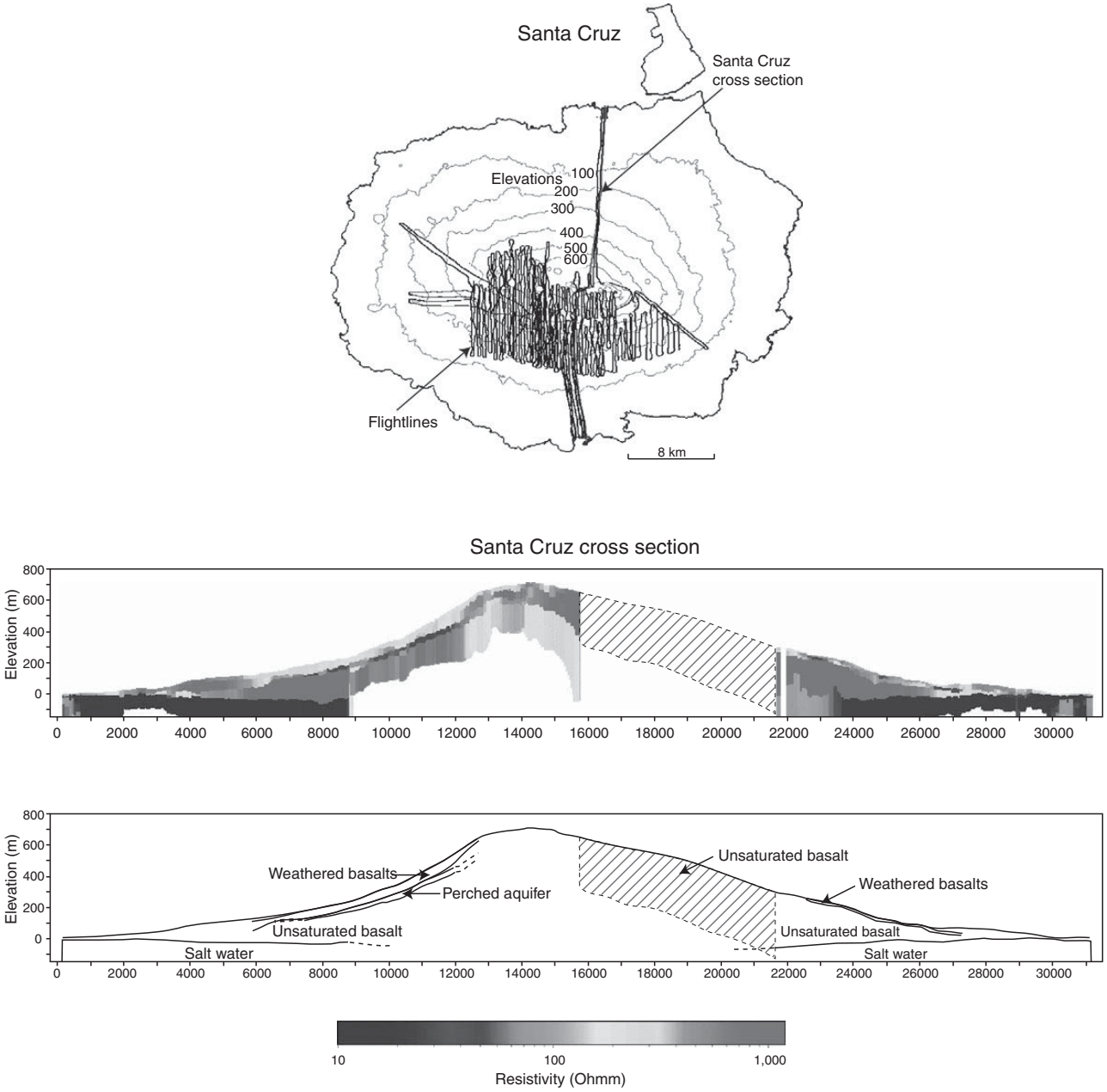

Figure 8.31 (Top panel) SkyTEM flight lines over Santa Cruz island. Contour levels in meters above sea level; (middle panel) resistivity profile along the north–south cross-section; (bottom panel) hydrogeological interpretation of the AEM data. After Auken *et al*. (2009).

series of 1-D local inversions is used to determine the subsurface conductivity structure. The northern leeward side of the island is found to exhibit very low conductivity and thus has a low hydrogeological potential. A perched aquifer at ~ 80–100 m depth may exist on the windward side. The AEM inversions also suggest that intruded seawater underlies the periphery of the island. The geophysical data cannot resolve the presence of possible freshwater lenses above the saltwater.